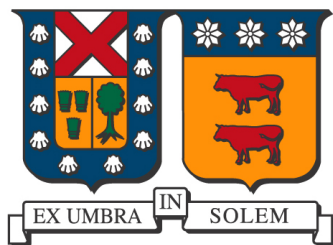


UNIVERSIDAD TÉCNICA FEDERICO SANTA MARIA
DEPARTAMENTO DE FÍSICA



PhD Thesis

Modern detectors to study the Standard Model and beyond

Author:
Gerardo Vásquez Arenas

Supervisor:
Sergey Kuleshov

Valparaíso, 2017

Abstract

The increased necessity of experimental proof of physics beyond Standard Model (SM) and Dark Matter theories leads us to develop new detectors for high energy experiments, such as ATLAS with its upgrade (New Small Wheel project in particular), for the luminosity increase at LHC and a new experiment on SPS facilities at CERN called NA64; to search for Dark Matter on invisible (visible) decays of dark photons.

For these two experiments, detectors from the Physics department of the University Santa Maria in Valparaiso (Chile) have been built to be part on such enterprise. Characterizations and tests have been conducted with the use of particles beam (electrons, pions, muons and gamma rays) from the Experimental Area at CERN.

Dedication

Acknowledgments

Agradecimientos

Contents

1. Introduction	13
1.1. Interaccion of Radiation with Matter	13
1.2. Gas filled detectors	13
1.2.1. Production of Electron-Ion pairs	13
1.2.2. Diffusion and Drift of Charges in Gases	13
1.2.3. Regions of Operation of Gas Filled Detectors	13
1.3. Scintillation detectors	13
1.4. Calorimeters	13
2. Small-Strip Thin Gap Chamber	15
2.1. Introduction	15
2.1.1. High Luminosity Large Hadron Collider	15
2.1.2. ATLAS Detector	16
2.2. sTGC Description	18
2.2.1. Electric field simulation	20
2.3. Construction process	21
2.4. Gain uniformity measurements	24
2.4.1. Setup	25
2.4.2. Results	26
2.5. Stability under high rate	28
2.6. Spatial Resolution	31
2.6.1. Analysis Model	33
2.7. Pad efficiency	37
2.8. Summary	40
3. High count rate γ-ray spectroscopy with Brilliance380	41
3.1. Introduction	41
3.2. Counter Limit	41
3.3. High Radiation Source	41
3.4. Data Analisys	41
3.4.1. Multiple hits	41
3.4.2. Wavelets	41
3.4.3. Peak identification	42
3.5. Results	42

3.5.1. Spectrum	42
3.5.2. Gamma Flux Rates	42
4. Synchrotron radiation detector for e^- tagging	43
4.1. Introduction	43
4.2. NA64 experiment	43
4.2.1. Physics Motivation	45
4.2.2. Dark Photon signal	45
4.2.3. Detector	47
4.3. Synchrotron Radiation Detector	48
4.3.1. BGO	49
4.3.2. Pb+Sc	50
4.3.3. LYSO	50
4.4. Calibration	53
4.5. Energy and time resolution	54
4.6. Hadron rejection	54
4.7. Experimental Results	54
4.8. Summary	54
5. Conclusion	55
A. Appendix	57
A.1. Mechanical Measurements sTGC Module 0	57
A.2. PMT RT7525 Data Sheet	57
A.3. NA64 Experiment:Data structure	57
A.4. NA64 Experiemnt:DAQ system	57

1. Introduction

2 page

1.1. Interaccion of Radiation with Matter

5 pages

1.2. Gas fillld detectors

5 pages

1.2.1. Production of Electron-Ion pairs

1.2.2. Diffusion and Drift of Charges in Gases

1.2.3. Regions of Operation of Gas Filled Detectors

1.3. Scintillation detectors

3 pages

1.4. Calorimeters

4 pages

2. Small-Strip Thin Gap Chamber

2.1. Introduction

The aim of this chapter is to show the characteristics of the new detectors presented for the upgrade of ATLAS detector, and how they can achieve the requirements for the high luminosity events. The results of each test to characterize the detector are presented in this chapter.

2.1.1. High Luminosity Large Hadron Collider

The Large Hadron Collider (LHC), run by the European Organization for Nuclear Research (CERN, derived from *Conseil Européen pour la Recherche Nucléaire*) at the Franco-Swiss border near Geneva, a circular accelerator with 27km of acceleration pipes, is the largest scientific instrument ever designed and built for scientific research. It has been successfully commissioned in March 2010 for proton-proton collision with a 7 GeV center-of-mass energy.

The LHC is pushing the limits of human knowledge, enabling physicists to go beyond the Standard Model (SM): the enigmatic Higgs boson, the mysterious Dark Matter and the world of super symmetry are just three of the long-awaited mysteries that the LHC is working to unveil.

The announcement given by CERN on 4 July 2012 about the discovery of a new boson at 125-126GeV[1, 2], almost certainly the long awaited Higgs particle, is the first fundamental discovery, hopefully the first of a series, that the LHC can deliver.

Such discovery was made possible thanks to the general-purpose detectors ATLAS and CMS, both located at 4 interaction points together with the detectors ALICE and LHCb.

	Period	Energy \sqrt{s}	Luminosity \mathcal{L}	Integrate \mathcal{L}
Run I	2010-2012	7-8 TeV	$6 \times 10^{33} \text{ cm}^{-2}\text{s}^{-1}$	25 fb^{-1}
LS1	2013-2014	Go to design energy, nominal luminosity, bunch spacing	25ns	
Phase 0	2015-2018	14 TeV	$1 \times 10^{34} \text{ cm}^{-2}\text{s}^{-1}$	75 fb^{-1} to 100 fb^{-1}
LS2	2019-2020	Upgrade muon spectrometer;NSW,LAr Calorimeter & FTK		
Phase 1	2021-2023	14 TeV	$2 \times 10^{34} \text{ cm}^{-2}\text{s}^{-1}$	$\sim 350 \text{ fb}^{-1}$
LS3	2024-2025	New Inner Tracker and trigger architecture		
Phase 2	2026-2030	14 TeV	$5 \times 10^{34} \text{ cm}^{-2}\text{s}^{-1}$	$\sim 3000 \text{ fb}^{-1}$

Table 2.1: LHC Schedule

2.1.2. ATLAS Detector

The ATLAS detector is a general-purpose detector, designed to explore proton-proton collisions at center of mass up to $\sqrt{s} = 14\text{GeV}$ in the Large Hadron Collider (LHC) at the European Laboratory for Particle Physics (CERN). It is aiming to understand the foundations of matter and forces, in particular the nature of mass in a broad physics program. The ATLAS detector was built with the ability to discover the Higgs boson over a wide mass range. It can also perform searches for the production of heavy particles that would indicate physics beyond the Standard Model, such as super symmetric particles, as well as searches for other massive objects.

To be able to detect such important and rare events, this machine has multiple and complex detector systems. In the central part of this cylinder lies the Inner Detector, the first part of ATLAS to see the decay products of the collisions, and as such, very compact and highly sensitive component. It consists of three different systems of sensors, all immersed in a magnetic field parallel to the beam axis. The **Inner Detector** measures the direction, momentum, and charge of electrically-charged particles produced in each proton-proton collision. The next part is the Calorimeter (red and green on figure 2.1), which measures the energy of a particle when it loses its energy as it passes through the detector. It is usually designed to stop entirely or “absorb” most of the particles coming from a collision, forcing them to deposit all of their energy within the detector. Calorimeters typically consist of layers of “passive” or “absorbing” high-dense material -for example, lead-interleaved with layers of an “active” medium such as solid lead-glass or liquid argon.

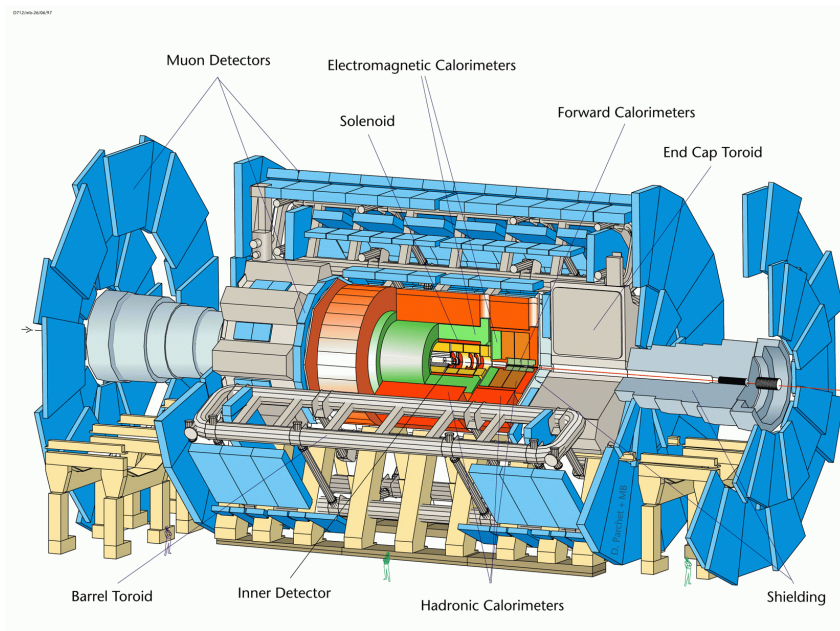


Figure 2.1: ATLAS detector, Muon Spectrometer (in blue)

Electromagnetic calorimeters measure the energy of electrons and photons as they

interact with matter. Hadronic calorimeters sample the energy of hadrons (particles that contain quarks, such as protons and neutrons) as they interact with atomic nuclei. The components of the ATLAS calorimetry system are: the **Liquid Argon (LAr) Calorimeter** and the **Tile Hadronic Calorimeter**.

Calorimeters can stop most known particles except muons and neutrinos. Muons are particles that usually pass through the Inner Detector and Calorimeter undetected, they can penetrate through large amount of material without any strong interaction, they have long lifetime, therefore, can be considered as stable particles within detector's volume, offering lepton decay channels for heavy objects as:

ADD lepto-production from heavy particles

To detect these particles, the ATLAS detectors use the **Muon Spectrometer**, made up of 4.000 individual muon chambers (different types of drift chambers) which are in charge of identify each one of these muons. However, it is only possible to measure its momentum with the help of the **Magnet System**, made of three sections; the **Central Solenoid Magnet** with 2T magnetic field bends the charged particles for momentum measurement near the interaction points, helping the Inner Tracker system, the **Barrel Toroid** bends the particles with low transversal momentum, and the **Endcap Toroid** with 4T magnetic field takes part in the high transverse momentum.

Coordinate system

A common coordinate system is used through ATLAS. The interaction point is defined as the origin of the coordinate system. The z-axis runs along the beam line. The x-y plane is perpendicular to the beam line and is referred to as the transverse momentum, p_T . The positive x-axis points from the interaction point to the center of the LHC ring; the positive y-axis points upward to the surface of the earth. The detector which is located half at positive z-values is referred to as the “A-side”, to the other half the “C-side”. The transverse plane is often described in terms of $r - \phi$ coordinates. The azimuthal angle ϕ is measured from the x-axis, around the beam. The radial dimension, r , measures the distance from the beam line. The polar angle θ is defined as the angle from the positive z-axis. The polar angle is often reported in terms of pseudorapidity, defined as $\eta = -\ln \tan(\theta/2)$. The distances ΔR is defined in $\eta - \phi$ space as $\Delta R = \sqrt{\Delta\eta^2 + \Delta\phi^2}$.

Detector Upgrade

To fulfill the LHC program (in table 2.1), and in order to benefit from the expected high luminosity performance that will be provided by the Phase-I upgraded LHC, the first station of ATLAS muon end-cap system (Small Wheel, SW) will need to be replaced. The **New Small Wheel (NSW)** will have to operate in a high background radiation region (up to 15 kHz/cm^2 of photons, and 75 Hz/cm^2 of neutrons is expected) while reconstructing muon tracks with high precision as well as furnishing information for the Level-1 trigger. These performance criteria are demanding. In particular, the precision reconstruction of tracks for offline analysis requires a spatial resolution of about $100\mu\text{m}$, and the Level-1 trigger track segments have to be reconstructed online with an angular

85 resolution of approximately 1mrad.

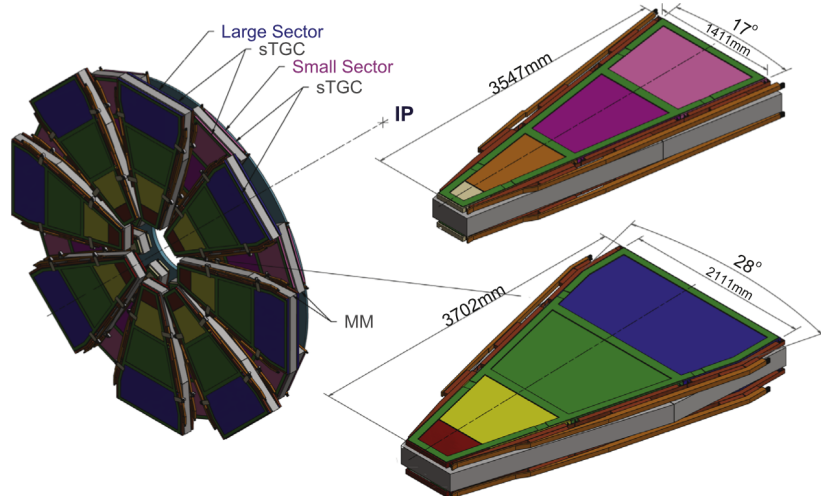


Figure 2.2: New Small Wheel

86 The NSW will have two chamber technologies, one primarily devoted to the Level-1
 87 trigger function (small-strip Thin Gap Chambers, sTGC) and the other one dedicated
 88 to precision tracking (Micromegas detectors, MM). The sTGC are primarily deployed for
 89 triggering given their single bunch crossing identification capability. The MM detectors
 90 have exceptional precision tracking capabilities due to their small gap (5mm) and strip
 91 pitch (approximately 0.5mm). Such a precision is crucial to maintain the current ATLAS
 92 muon momentum resolution in the high background environment of the upgraded LHC.
 93 The MM chambers can, at the same time, confirm the existence of track segments found
 94 by the muon end-cap middle station (Big Wheels) online. The sTGC also has the ability
 95 to measure offline muon tracks with good precision, so the sTGC-MM chamber technology
 96 combination forms a fully redundant detector system for triggering and tracking both for
 97 online and offline functions. This detector combination has been designed to be able to
 98 provide excellent performance for the eventual High Luminosity LHC upgrade.

99 2.2. sTGC Description

100 The small-Strip Thin Gap Chamber (a.k.a sTGC) is a multi-wire proportional chamber
 101 (MWPC), a detector type with a relatively old technology, its successful introduction to
 102 detector systems in 1968, it gave the Nobel prize to George Charpak in 1992. Those
 103 devices have been a major ingredient to detector systems since they can achieve spatial
 104 resolution of several microns, and have typical time resolution of about 50ns. The sTGC
 105 has been design to exploit these features, working with a cathode-anode pitch smaller
 106 than the anode-anode pitch, mostly based on the design of the Thin Gap Chamber[3],
 107 with thinner strips as the main improvement from the previous version. The TGC

technology has been used since 1988 in OPAL experiment and is currently part of the muon spectrometer in ATLAS. 108
109

This new chamber has the advantage of having a 3.2mm strip-pitch (2.7mm strips and 0.5mm gap) compare to the 6mm from the previous TGC, which explains the *small-strip* prefix. 110
111
112

Chambers with different strips sizes were built and tested under pion beams, and the 3.2mm was chosen as the best option[4] to provide a resolution better than $100\mu\text{m}$. This change will improve the measurement of charge centroid position by charge interpolation. 113
114
115

To improve the time response, the cathode surface resistivity has been reduced by a factor 10, to reduce charge accumulations on the cathode when chamber operates at high rate, lowering from $1\text{ M}\Omega/\square$ to $100-200\text{k}\Omega/\square$ resistivity on the graphite layer. At the same time, cathode-readout plane (strips or pads) distance was reduced to 0.1mm(1.6mm before) to increase the capacitive coupling by 10, therefore the RC factor keeps unchanged. 116
117
118
119
120

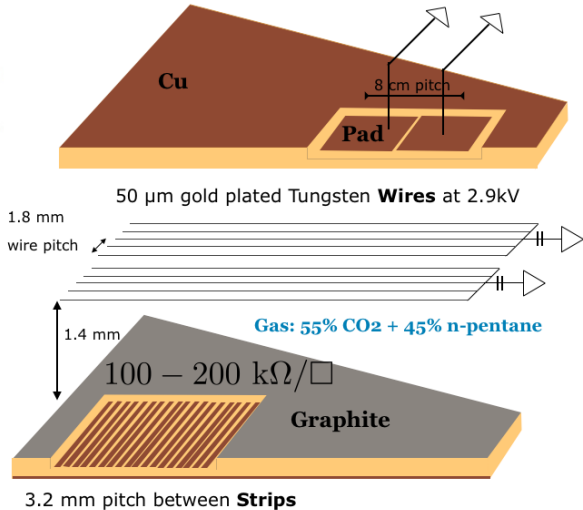


Figure 2.3: Single plane sTGC

The sTGC is made of two resistive cathodes planes, with copper readout plane with strips on one layer and the other one with pads, with $8 \times 12\text{cm}^2$ area used for fast pattern recognition of tracks to select strips for read out. This represents a big advantage compare to the TGC, which does not have this feature. 121
122
123
124

The cathodes are made of FR4 with 1.6mm of thickness, where $100\mu\text{m}$ of copper is etched for strips (pads), pressed with a $100\mu\text{m}$ of FR4 over it and then sprayed with graphite to provide superficial resistivity. 125
126
127

The anodes are golden tungsten wires of $50\mu\text{m}$ diameter, distributed at 1.8mm between each other and a gas gap of 2.8mm. To work with such geometry, several tests were made to find the proper gas mixture[5]. The most suitable mixture has been found to be 55% of the well known carbon dioxide(CO_2) as a quenching gas as a primary ingredient and 45% of n-pentane($\text{n-C}_5\text{H}_{12}$), which allow it to work in a limited proportional region[6](see Section 1.2.3). The latest ingredient; n-pentane, can absorb UV photons due to its many 128
129
130
131
132
133

¹³⁴ molecules degree of freedom, hence it prevent the chamber going into a Geiger mode.

¹³⁵ 2.2.1. Electric field simulation

¹³⁶ Motivated by gaining better understanding of the detector operational mechanisms,
¹³⁷ dedicated simulations studies using gaseous detector simulation tools have been performed.
¹³⁸ The main simulation tool used is Garfield [7, 8] software package. This set of libraries
¹³⁹ allow to calculate the electrical field with geometrical configuration as drift chambers.

¹⁴⁰ The simulation uses a coordinate system where x is along the strips, y defines the
¹⁴¹ chamber depth and z is along the wires.

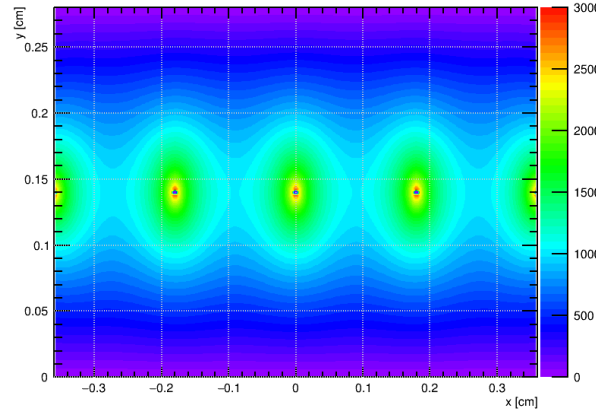
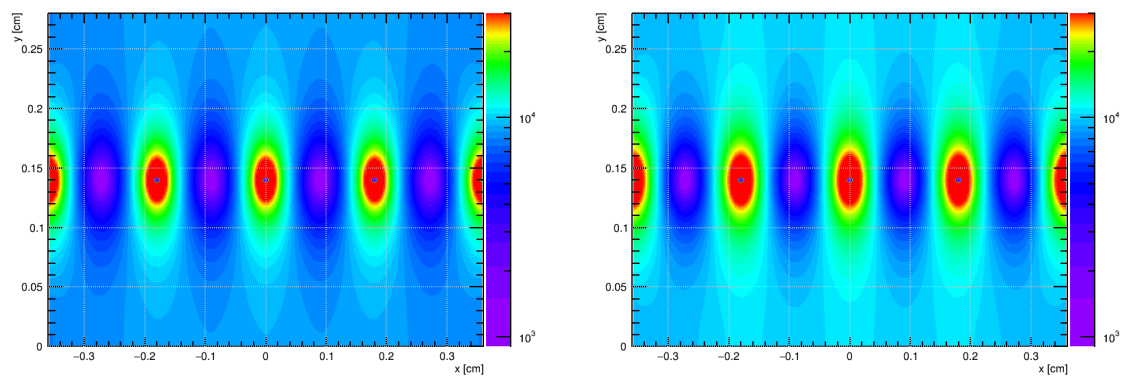


Figure 2.4: Equipotential lines, anode at 2900V



(a) Electrical field, anodes at 2500V

(b) Electrical field, anodes at 2900V

Figure 2.5: The electric field map in the x-y plane for a typical operating high voltage 2900V and 2500V.

¹⁴² Both contour plots on figure 2.5 represent the magnitude of the electrical field with
¹⁴³ scale of 1×10^3 V/cm to 1×10^5 V/cm with 50 steps. At the working potential 2.9 kV it
¹⁴⁴ is possible to observed a field strength of more than 1×10^4 V/cm over a 97% of the gas
¹⁴⁵ gap. The weakest field it is only in a small region in the middle of two neighboring wires.

2.3. Construction process

146

The main novelty on this detector is the high resolution obtained on x-axis due to the strip boards and the alignment between each chamber to get precision about $50\mu\text{m}$ and $30\mu\text{m}$ respectively.

It is important to discuss how is possible to achieve those numbers. Everything relies on how well those chambers are built and also how the cathodes boards (strips and pads) are fabricated.

The size of each chamber varies from 0.7 m^2 to 2 m^2 with around 1m long, where over 300-400 strips must be etched with a precision of $50\mu\text{m}$. A standard length for PCB boards is 70 cm. Extremely precautions must be taken to provide the precision and parallelism between each strips, in one of the biggest PCB board ever made.

The attempt of this sections is to give an idea of how the sTGC Quadruplets are built, mostly on the first module 0 produced by UTFSM, which is the QS1 (Quadruplet Small sector, part 1). Being the smallest detector to be produced for the NSW has some pros and cons. The main cons is related to the position of the QS1 inside the NSW, it is the closest one to the interaction point and as such, it gets the highest rate of particles. For the same reason, the position resolution is a key point and the high efficiency response under a high rate environment is a must.

Some pros are related to its size, with approximately 1.3 m long, 35 cm the small base and 75cm the large one of the trapezoidal shape, the sTGC QS1 can be handled without any problems during its construction.

Quality Control of cathode boards

167

The cathodes for the module 0 were made by an Italian company MDT, and since it was the first production, the review was done on-site.

The thickness of the board is measured in 19 points around the perimeter with a micrometer. The values of theses measurements must be within $1.4\text{mm}\pm25\mu\text{m}$. Exceeding this numbers leads to the partial rejection of the cathode boards, however if there is a single point deviation of less than $35\mu\text{m}$ from the average, it could be used in combination with another cathode board that does not have the same local deviation. The raw data is found in appendix X.

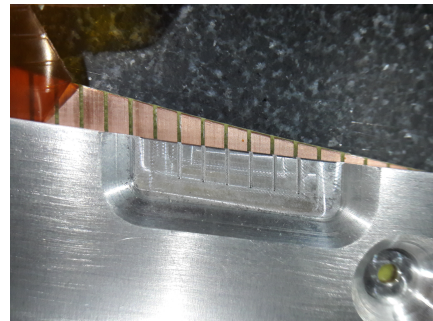
An electrical test is done with a multimeter, to check if there is any short circuit between strips or pads depending on the cathode board.

The last step and the most important is the dimensional control; it is performed on a granite table, with 2 pins that match the brass inserts on the cathode and a special caliper. An Aluminum-ruler machined (see figure 2.6a) with a precision of $30\mu\text{m}$ at 20 Celsius degrees is used as caliper. Above the cathode board the misalignment is measured. The caliper is an Aluminium ruler machining with a precision of $30\mu\text{m}$ at 20 Celsius degrees, it has the same strip pitch for the first and last five strips and to avoid any parallax the thickness is the edge for those strips is 1mm. Looking with a lens glass around this point it possible to detect some misalignment between this two strips (caliper and cathode board). A photography is taken and analyze to calculate this misalignment. For such distance

¹⁸⁷ (about 1 m long) some precaution must be take, considering the expansion coefficient for
¹⁸⁸ both material. Machining with a precision of $30\mu\text{m}$ measure at 20 Celsius degrees.



(a) Al-ruler used to check shift over the last strips.



(b) Zoom-in Comparing strip position

Figure 2.6: Strip control with Al caliper

¹⁸⁹ Cathode preparation

¹⁹⁰ Once the cathodes pass all the dimensional control, those had to be cleaned with
¹⁹¹ Acetone and Isopropyl alcohol and placed on a granite table (with a flatness better than
¹⁹² $30\mu\text{m}$) with a vacuum system underneath. They have to be fixed on the edges with metal
¹⁹³ jigs which have marks for the internal wire support or chamber division.

¹⁹⁴ The places which are not sprayed with graphite, like the wire support and the edges,
¹⁹⁵ are covered with a 3.5mm black tape on the designated wire support locations across the
¹⁹⁶ board. To prevent spraying graphite on the places where there will be glue a blue tape
¹⁹⁷ must be placed on the edges.

¹⁹⁸ Graphite spraying

¹⁹⁹ A key point for this process is to prepare the “painting”, a mixture of Graphite-33
²⁰⁰ with Plastik-70 bonding agent. The graphite must be agitated for at least 2 hours before
²⁰¹ mixing with Plastik-70. A proper ratio of 1500g Graphite and 540g Plastik is mixed
²⁰² during 2 hours before spraying. The mixture must be is continuing mixing while

²⁰³ A spraying machine is in charge of this process, and meanwhile temperature and
²⁰⁴ humidity must be controlled. After the cathode is painted, the superficial resistivity is
²⁰⁵ measured on the edges. Values must exceed $100\text{k}\Omega/\square$ otherwise the cathode needs to be
²⁰⁶ sprayed again.

²⁰⁷ Polishing

²⁰⁸ In order to ensure an uniform resistivity across the chamber, the cathode is visually
²⁰⁹ divided in to 5x6 sections. Inside each section, the resistivity is measured on 5 to 7
²¹⁰ points with a probe. Simultaneously the cathode is brushed in the same orientation as

the wires. The brush must be done carefully, without over-polishing areas, since once
211
resistance drops down, nothing will bring it back up.
212

Glue internal parts

213

After removing all the blue and black tapes, all the internal parts (buttons, wire
214
support, etc. are glued to provide mechanical support to the gas gap.
215

The wire support and the buttons help the chamber not to bend due to gravity and
216
not to create a catenary effect. The external frames provide the 1.4mm height for the gas
217
gap. All these part are cleaned with isopropyl alcohol, While the glue, a type of epoxy
218
(2011-Araldite) is prepared, all these parts are cleaned with isopropyl alcohol. This glue
219
will not only fix the parts, it will also fill the surfaces where these parts are less thick
220
than requested.
221

Winding wires

222

A flat table which can spin around one axis is used to wind the cathodes board. On
223
each side of the table, one cathode with all the internal parts is tight with metal clamps
224
on the edges. At the same time, vacuum is applied underneath to ensure the flatness
225
of the cathode. A winding machine places each wire at 1.8mm distance from each other
226
with $50\mu\text{m}$ precision.
227

After the process is completed, all the wires are soldered in batches of 10 over the
228
wire-rulers with $10\text{M}\Omega$ resistor to the high voltage line. Later on, the remaining wire
229
can be cuted and the metal clamps around the edges can be removed.
230

Detector Assembly

231

Once the cathodes are winded and all wires are soldered, the Pad cathode board is
232
cleaned with clean water and dried with clean air. The board is placed on the granite table
233
(with vacuum underneath) to be tested with high voltage. It is necessary to monitor the
234
current from the cathode while the voltage is increased. It starts with 100V and reaches
235
3000V, with steps of 100V. The current should never reach a value higher than $1\mu\text{A}$. If
236
it does, the cathode needs to be checked carefully, to remove dust or glue which create
237
sparkles.
238

Reaching the nominal current, the strip cathode board is placed against the pad cathode
239
board carefully. An Aluminium frame with a silicon rubber is placed on top to isolate
240
the chamber from the environment. Afterwards, vacuum is applied to this chamber and
241
only CO_2 is flushing inside the chamber.
242

The power supply is turned on and no sparkles (monitoring the current) must be
243
found.
244

In order to prevent dust entering the chamber the glue is prepared to close the chamber
245
immediately. Upon completion of the process, a single chamber is built.
246

A doublet is assembled with two single chamber glued with a honeycomb paper.
247
Repeating the process with two doublets, the quadruplet is built.
248

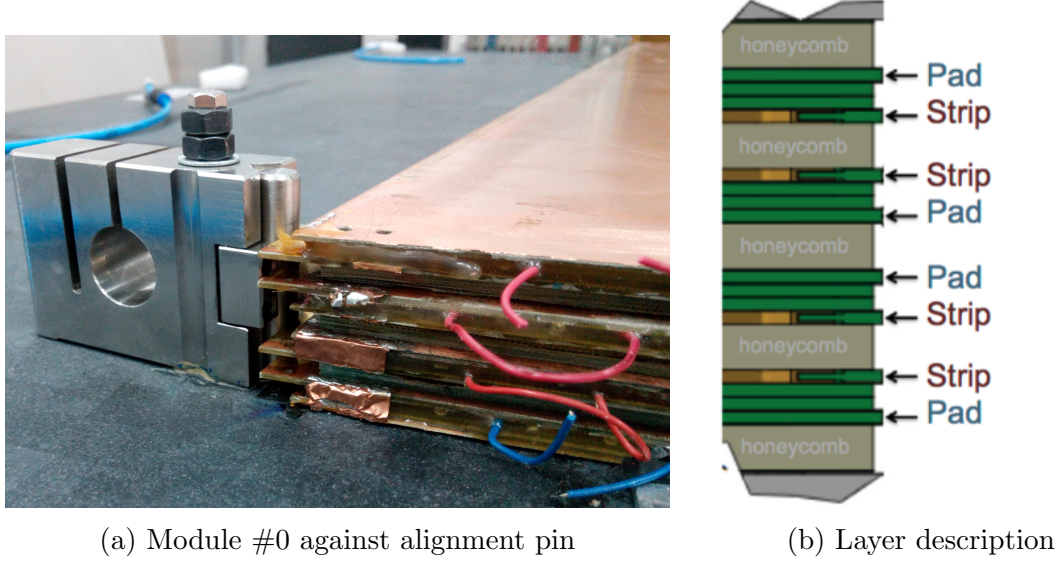


Figure 2.7

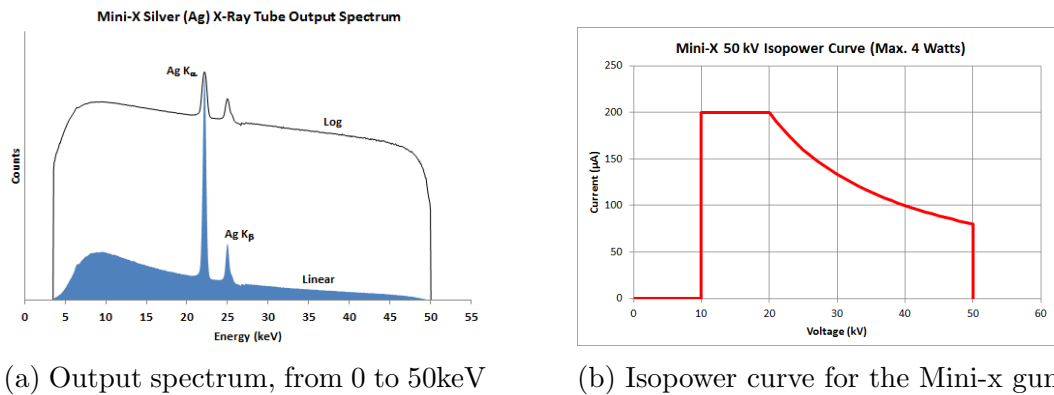
249 2.4. Gain uniformity measurements

250 After the chambers are built, it is important to look for any malfunctioning. A
 251 primitive test to check the behavior of the detector, is to use a radiation source and move
 252 it across the sensitive area and measure the current draw from the power supply. This
 253 test will give us the first answer of the gain of our detector.

254 In this test, it is important to understand what can produce variation on the gain.
 255 There are two main ingredients that can produce gain variations on wire detectors. The
 256 first one is the “nature” gain fluctuations from the charge production in proportional
 257 counters which follow Polya distribution, however is less pronounced in limited-proportional
 258 mode such as sTGC working region.

259 The second one is related to the mechanical tolerances, this part is very well known since
 260 40 years as it is presented on Sauli’s book [9] about drift chambers and tell us:

- 261 ■ A diameter variations of the wire about 1% (fabrication precision) will result on a
 262 3% change in the gain.
 - 263 ■ $100\mu\text{m}$ difference in the gas gap thickness(2.7mm) results in about 15% change on
 264 the gain.
 - 265 ■ The effect of a wire displacement of about $100\mu\text{m}$ of a wire plane results in 1% in
 266 the charge of the two adjacent wires which with a gain of $\sim 10^6$ will give a $\sim 10\%$
 267 change on the gain.
- 268 Taking all of this in consideration, it is expected to get a gain variation less than 20%
 269 according to the Construction manual[10].



(a) Output spectrum, from 0 to 50keV (b) Isopower curve for the Mini-x gun

Figure 2.8

The amount of current measured from the power supply it will be considered as gain reference, while the detector is irradiated with x-rays. The test is performed under two different working points (bias voltage), 2500V (low gain) and 2900V, the operational voltage.

For such test the x-ray source is used thanks to the advantages:

- Mostly mono-energetic photons.
- Variable photon intensity: Limiting the current from the tube from 1 μ A to 200 μ A can provides different rates.
- Variable photon energy: Varying the breaking voltage of electrons inside the x-ray gun from 10 kV to 50 kV.
- Different spot size: with a set of collimator it is possible to irradiate only interesting area.

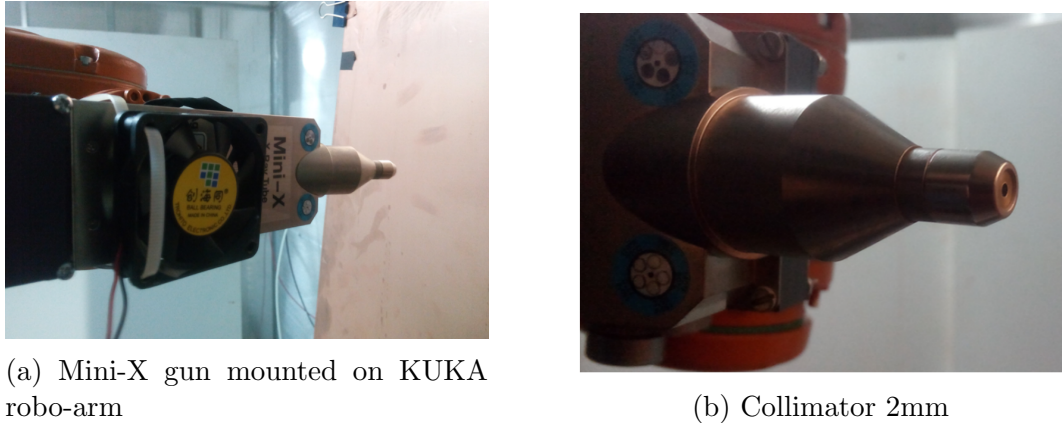
2.4.1. Setup

To perform such test, a x-ray gun called Mini-X[11] from Amptek is used, with silver (Ag) as transmission target and with a beryllium (Be) end-window is used.

The gun is mounted on a KUKA robo-arm (see Fig.2.9a), with a 5 degrees collimator providing a 4 mm^2 spot size at a proper distance. The robo-arm provide the x-y movement to scan the whole sensitive detector area, moving from the small base to the large base along the wires at step of 1.2 cm/s. Each y-movement were separated for 5 cm, being not the most suitable distance to irradiate the whole detector, but it was choose to work properly with the x-ray gun at 45 μ A, 50keV energy (see figure 2.8b) without overheating the gun.

A NIM HV Power Supply Module CAEN 1470 was used to power the chambers. The power supply (PS) was controlled by USB with the CAEN HV Wrapper Library. The current registered from the PS was written in a ASCII file for further analysis. The sampling rate used from the PS was 1 per second, giving the current average during this period.

The test is taken in approximately one hour, irradiating one chamber at the time.



(a) Mini-X gun mounted on KUKA robo-arm

(b) Collimator 2mm

Figure 2.9

298 Since the detector is already built as a quadruplet, it has to turn over to irradiate
 299 the other face of it. Hence, only the external layers (chambers) are irradiated directly
 300 without having an chamber to provide an screening effect.

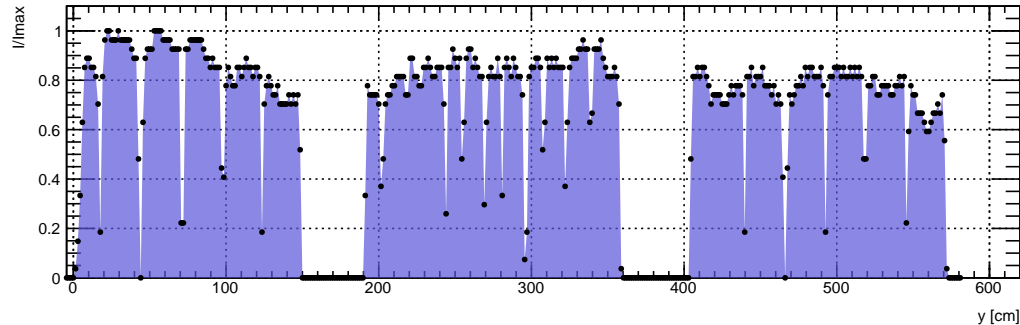


Figure 2.10: Relative current to the maximum, while the robo-arm is moved along the detector passing 3 times at different position across the wires (x-axis)

301 2.4.2. Results

302 At first glance, it is possible to observed the internal structure of the chamber with
 303 this test. Looking the plot 2.11 the current decrease when the gun is irradiating the
 304 places where the wire-supports are found. In theses places a small gas volume is present,
 305 therefore less electrons can drift to the wires, resulting in less current draw from the power
 306 supply.

307 If a better meshing of the irradiation places can be perform, the identification of the
 308 wire-supports and the chamber separation (small and large sector) can be obtained with
 309 good resolution, however, it can be obtained with this test, a width of 17 mm to 23 mm
 310 of theses internal parts, when the real size is 20 mm.

311 Interpolating the points (x, y, I) an overall picture can be obtained (figure 2.12a).
 312 The figure shows a line with high current resulting from a missing wire on the chamber

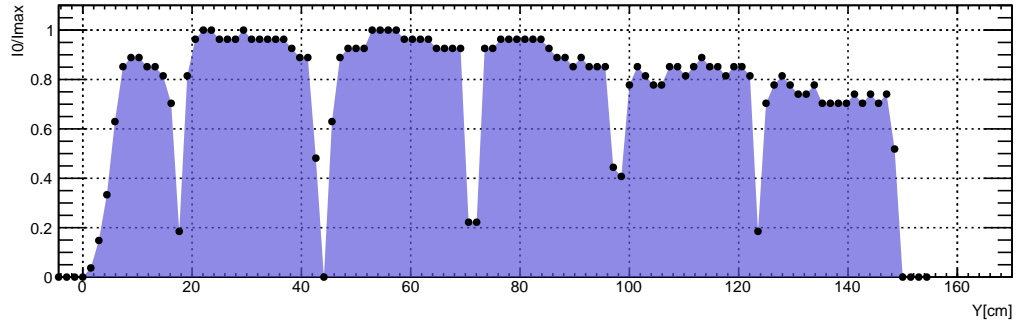
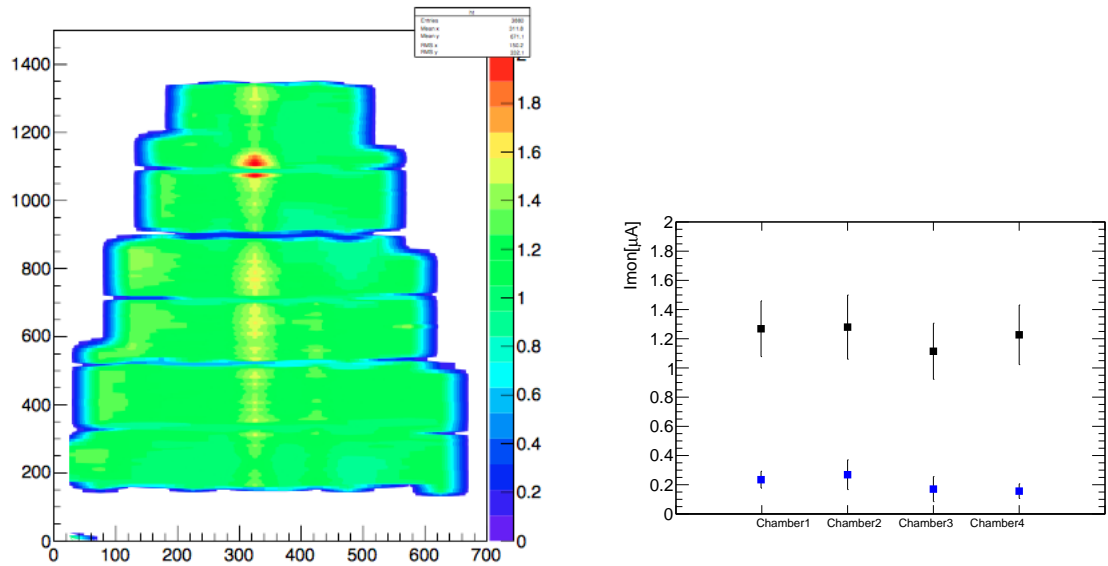


Figure 2.11: Moving across strips, wire-supports are present with minimum gain.

2. More charge is collected on the neighbors when a wire missing, resulting from a longer drift path. 313
314



(a) xy-scan chamber 2 sTGC Module #0: (b) Current draw at 2.5kV (blue) and 2.9kV(black)

Figure 2.12

The graph on figure 2.12b shows the average current from each chamber at two different working potential. The average is calculated only for the sensitive area, hence the places where the wire-support are present are not part from the average. The current on average at 2.5kV and 2.9kV are 200 nA and 1.2 μ A respectively. 315
316
317
318

The table 2.4 summarize the uniformity obtained, calculated as the RMS over the mean from the current draw distribution for each chamber. The four chambers have less than 20% of gain variation, which it was expected from the construction manual. 319
320
321

	Chamber 1	Chamber 2	Chamber 3	Chamber4
$\sigma/\text{mean}\%$	15.08%	17.18%	17.25%	16.64%

Table 2.2: Uniformity gain

322 2.5. Stability under high rate

323 One of the key feature of this detector is that must be able to work under high particles
 324 flow rates ($15\text{kHz}/\text{cm}^2$), and the first step is check either the device or its electronic
 325 components can handle this high rate.

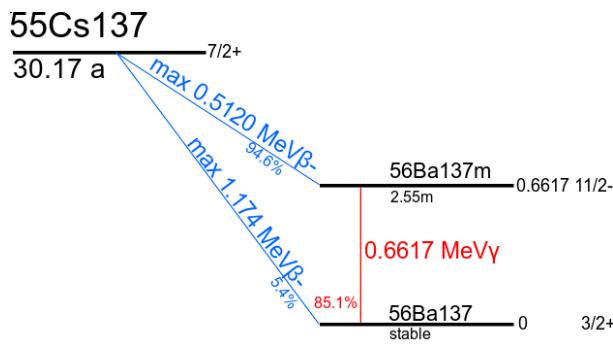


Figure 2.13: Cesium-137 Decay scheme.

326 For this purpose the module 0 was placed inside of a High Radiation Facility at CERN
 327 called GIF++[12]. The installation has a Cesium-137(Fig. 2.13) as a gamma source with
 328 an activity of approximately 14.9TBq (13.3TBq during the test, August 2016). A system
 329 of movable lead attenuators (figure 2.14) for large irradiation zone, allows attenuation
 330 factors between 1 and 5×10^5 in several steps.

331 In order to get the particle rate, a direct measurement setup was implemented with
 332 a small size ($16.2\text{ cm} \times 12.4\text{ cm}$ as sensitive area) sTGC as a **Monitor**. A LVDS (Low
 333 voltage differential signaling) logical signal from wires was obtained from an Amplifier
 334 Shaper Discriminator (ASD) board[13]. The ASD board provide the signal from 16 wires
 335 groups, all of them connected to a VME module (KEK ASD buffer) control the discriminator
 336 threshold from the ASD and convert the LVDS to NIM signal. The 16 LVDS signals are
 337 converted into two NIM logic signals. The two outputs from this modules are connected
 338 to an Scaler NIM n145 to provide the total rate on the **Monitor**.

339 The Module#0 and the Monitor were placed at 1.3m distance from the source. Both
 340 connected in series to the same gas line, the temperature and pressure was recored to
 341 keep in track the working voltage, where most of the time the environmental conditions
 342 were 25 Celsius degree and 971mb .

343 The working potential for the chamber is 2850V at 1b . Since the gain is proportional to
 344 E/P , the voltages must be increase in 2.9% to correct de lower pressure, giving a 2935V
 345 as the new working point in this environment.

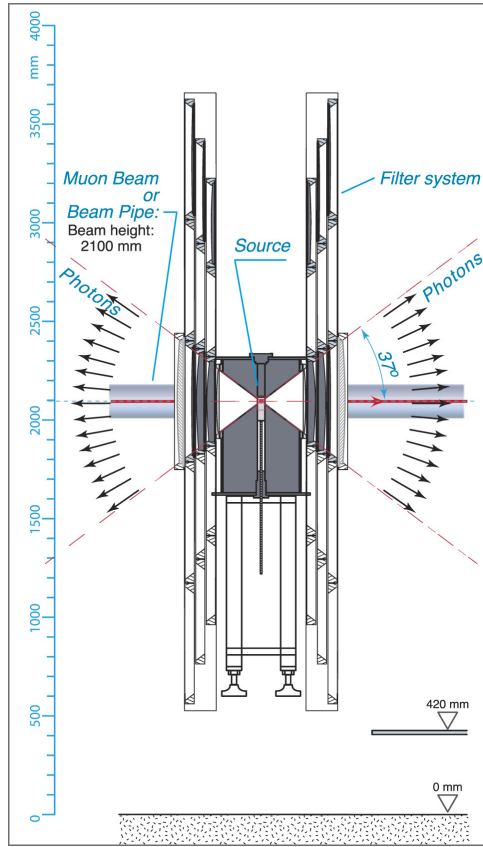


Figure 2.14: Irradiator with filter system. Three different rows with three lead (Pb) layer each one with different thickness helps to provide multiples rates for the facility.

To achieve the background rate for ATLAS (15kHz/cm²), the Monitor must register more than 2680 kHz if the sensitive area is considered. The sensitive area is calculated as the total area 200 cm² times the amount of wires group connected to the ASD (16 over 18).

Four different attenuation factors were registered, where on Figure 2.15a, is possible to observed two set of data over than the expected rate (red and blue). The other two set of data emphasizes the *plateau* reached over 2.7 kV. At the same time, the highest rate shows an inefficiency on voltages over 2.8 kV and the *plateau* is lost. Therefore, the data set with attenuation 2.2 (in red) is our reference.

Multiplying the attenuation factors with each data set (Figure 2.15b) will give us the expected rate with no filters, however, the data set with factor 1 has 5 MHz at working potential, while the expected rate is 6.6 MHz, resulting in an inefficiency of about 75%. The flow rate recorded in this data set is 28 kHz/cm², almost the double than expected. At the same time, the interest should go on the red line (attenuation factor of 2.2) which represent the background level expected for ATLAS with an estimated flow rate of 16.2 kHz/cm² with an efficiency approximately of 93% respect to the lowest rates.

Once the Monitor is set, the quadruplet is connected to the high voltage power supply. Each layer is internally divided in two sections, a small sector (S0) and large sector (S1).

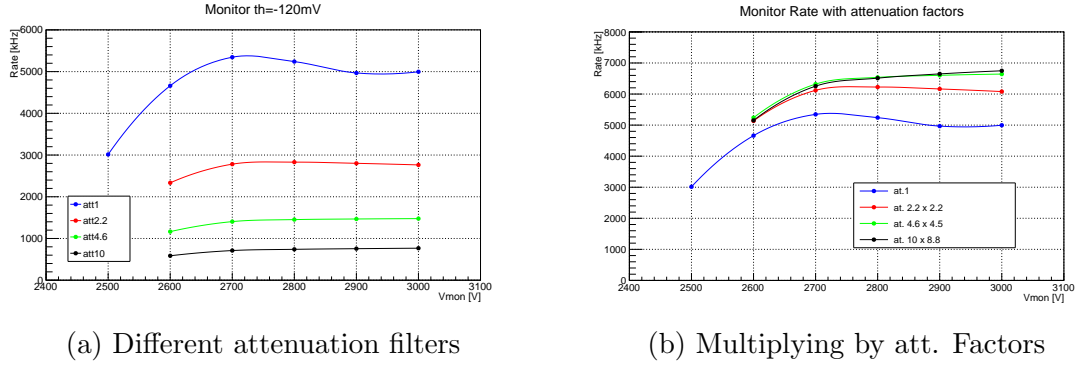


Figure 2.15: Rate on Monitor

364 Each one of these sector is powered independently on each channel from the CAEN High
 365 Voltage power supply A1833P (4 kV/2 mA). The current from each layer (two sectors
 366 each one) was recorded with a resolution of 0.1 μ A. Four different attenuation filters were
 367 applied, and the results are shown in Figure 2.16.

$$\Delta\% = \left(1 - \frac{I_1/I_0}{A_1/A_0} \right) * 100 \quad (2.1)$$

A_1/A_0	Layer 1		Layer 2		Layer 3		Layer 4		
	Filter	I_1/I_0	$\Delta\%$	I_1/I_0	$\Delta\%$	I_1/I_0	$\Delta\%$	I_1/I_0	$\Delta\%$
		10	2.49	3.5	3.02	6	3.01	3.8	3.08
	4.6	2.34	9.3	2.87	0.7	2.73	12.7	2.87	17.3
	2.2	2.29	11.2	2.79	2.1	2.68	14.4	2.67	23.1
	1	2.22	14	3.02	6	2.45	21.7	2.49	28.2

Table 2.3: Comparison between sensitive area ratio (A_1/A_0) from large and small sector with the ratio of current (I_1/I_0) at 2.9kV. A percentage difference column ($\Delta\%$ defined in equation 2.1) is calculated to highlight the incremental disagreement as the gamma rate increase.

368 These results shows an linear dependence of voltage, with lower resistance as the rate of
 369 particles is increased. It is important to notice, each wire group is connected to a $10\text{ M}\Omega$
 370 resistor, however not all the wires have the same length (the chamber has a trapezoidal
 371 shape), having lower voltage drop from the external groups where the wires are shorter
 372 (collecting less charge).

373 The table 2.3 compare the area ratio between the internal sections of each chamber
 374 with the current registered for each set of measurements. The effect on dropping voltage
 375 appears to be the explanation of the incremental disagreement from the area ratio as the
 376 rate increase. The larger percentual difference is for the Layer 4 where the larger section
 377 is bigger than the previous ones, hence, the current ratio is lower.

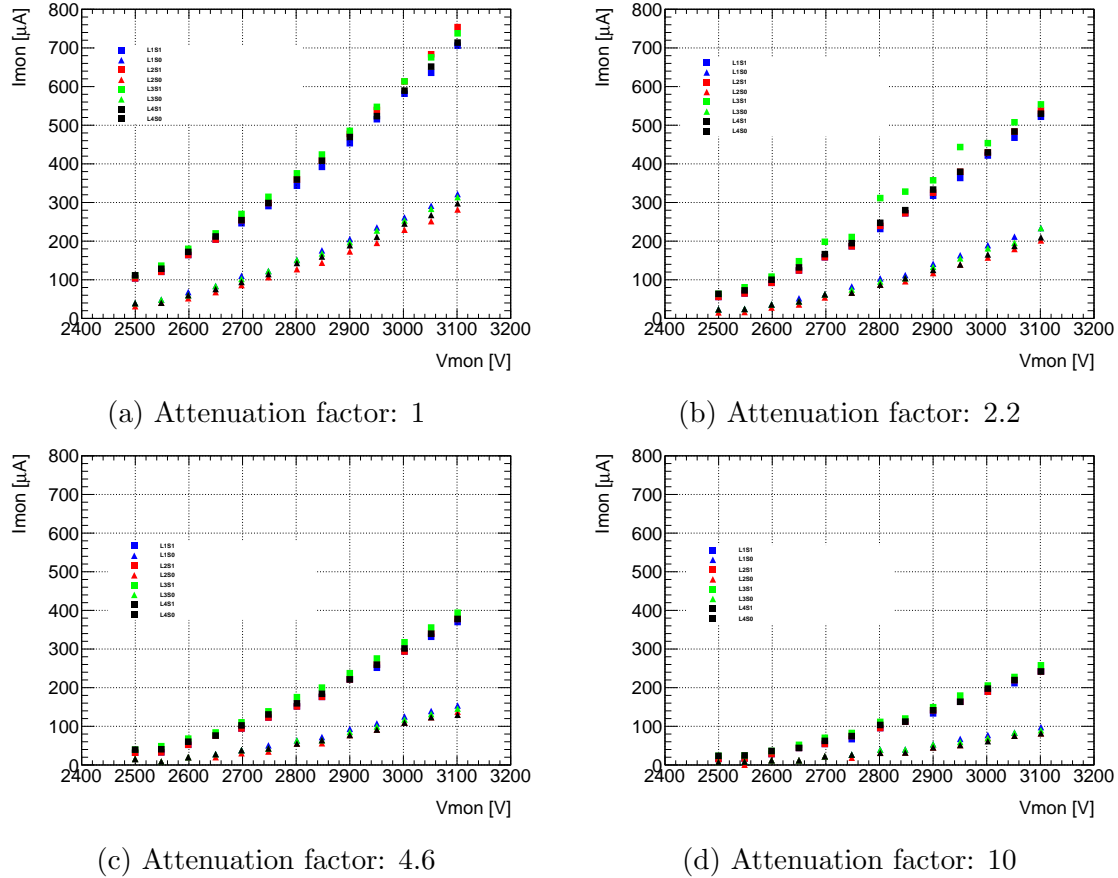


Figure 2.16

2.6. Spatial Resolution

379
380
381
382
383
384
385
386
387
388
389
390
391
392
393

In order to achieve the precision reconstruction of tracks (offline) with a spatial resolution of about $100\mu\text{m}$ per sTGC layer, and fast trigger on the region of interest (ROI) with Pads, two test beams were done.

In the spring of 2014, the Weizmann Institute of Science in Israel built the first full-size sTGC quadruplet detector of dimensions $1.2 \times 1.0\text{m}^2$. This prototype consists of four sTGC strip and pad layers and is constructed using the full specification of one of the quadruplets to be used in the NSW upgrade (the middle quadruplet of the small sector). The first test beam experiment took place at Fermilab with one goal in mind, determine the position resolution of a full-size sTGC.

par EUDET pixel telescope were use as a reference for measure beam position, using the technology of 6 Minimum Ionizing MOS Active Pixel Sensor (Mimosa26) detectors with $\approx 5\mu\text{m}$ position resolution. Three in front of the beam, and three after the sTGC as is shown in fig.2.17 with 15cm between them and 64cm between each arm. Each Mimosa26 detector has an active area of 2.24cm^2 made of CMOS pixel matrix of 576 rows and 1152 columns with $18.4\mu\text{m}$ pitch.

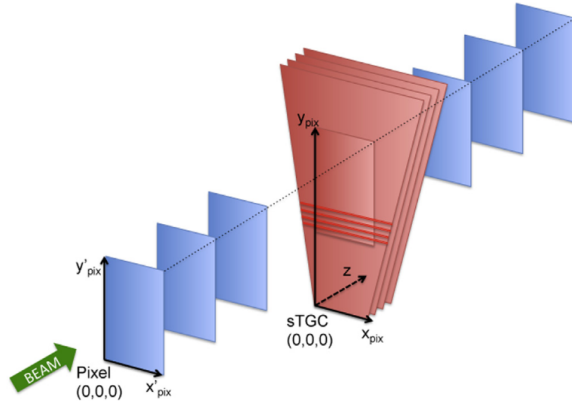


Figure 2.17: Schematic diagram of the experimental setup at Fermilab and coordinate systems used. Three layers of silicon pixel sensors are positioned before and after the sTGC detector. The dimensions are not to scale.

394 A 32GeV pion beam was used at rate of 1kHz over a spot of 1cm^2 giving to the sTGC
 395 a very precise pion trajectory thanks to the EUDET telescope. Event triggering was
 396 controlled by a custom Trigger Logic Unit (TLU). The TLU received signals from two
 397 $1\times 2\text{cm}^2$ scintillators placed in front and behind the telescope. The TLU generated the
 398 trigger signal that was distributed to the telescope and the sTGC readout electronics,
 399 which consist of a first application-specific integrated circuit (ASIC) called VMM1 which
 400 has the ability to read out both positive (strips, pads) and negative (wires) polarity
 401 signals, on 64 individual readout channel. The VMM1 analog circuit features a charge
 402 amplifier stage followed by a shaper circuit and outputs the analog peak value (P) of the
 403 signal. The readout of the ASIC is zero suppressed and thus only peak values of channels
 404 with signals above a predefined threshold are read and at the same time the VMM1 may
 405 be programmed to provide the input signal amplitude of channels adjacent to a channel
 406 above threshold (neighbor-enable logic), which in case of the strips is strictly necessary
 407 due to the cluster size is about 3-5 strips.

408 The precise position of a charged particle traversing an sTGC gas volume can be
 409 estimated from a Gaussian fit to the measured charge on adjacent readout strips (referred
 410 to as strip-clusters from here on). Given the strip pitch of 3.2mm and sTGC geometry,
 411 charges are typically induced on up to five adjacent strips. The spatial sampling of the
 412 total ionization signal over a small number of readout channels means that a precise
 413 knowledge of each individual readout channel baseline is necessary in order to achieve
 414 the best possible measured spatial resolution. The baseline of each individual readout
 415 channel was measured by making use of the neighbor-enabled logic of the VMM1 and
 416 its internal calibration system. Test pulses were sent on one readout channel with the
 417 neighbor-enabled logic on, and baseline values were obtained by reading out the analog
 418 peak values of the two channels adjacent to the one receiving a test pulse.

419 The silicon pixel hit positions were then used for reconstructing straight three dimensional
 420 charged-particle tracks. A track quality parameter was obtained for each fitted pion track

based on the χ^2 of the track-fit. A small value of the track quality parameter corresponds to a straight track and a cut on this parameter can therefore be used to mitigate multiple scattering which are not considered in this analysis. 421
422
423

2.6.1. Analysis Model

424

Pixel telescope analysis

425

In this model the intrinsic position resolution is obtained comparing the extrapolated beam trajectory from the pixel detectors with the measurements in each of the sTGC quad planes. Each layer is analyzed separately to reduce the effect of the multiple scattering and only tracks with $\chi^2 < 10$ are considered for the same reason. From fig.2.17 you can see that the y -axis is defined perpendicular to the strips, therefore sTGC strip-clusters provide measurements of the particle position in the y -direction(y_{sTGC}). The position resolution is directly related to the profile of induced charge on the strips. The particle position is estimated from a Gaussian fit to the induced charge distribution on the strips. The neighbor-enabled logic of the VMM1 was used. Strip-clusters with induced charge in either 3, 4 or 5 adjacent strips are selected. 426
427
428
429
430
431
432
433
434
435

The pixel telescope tracks provide both coordinates, x_{pix} and y_{pix} at the position of the sTGC layer studied. The spatial resolution measurement is obtained by fitting the residual distribution y_{sTGC} and y_{pix} with a Gaussian model. 436
437
438

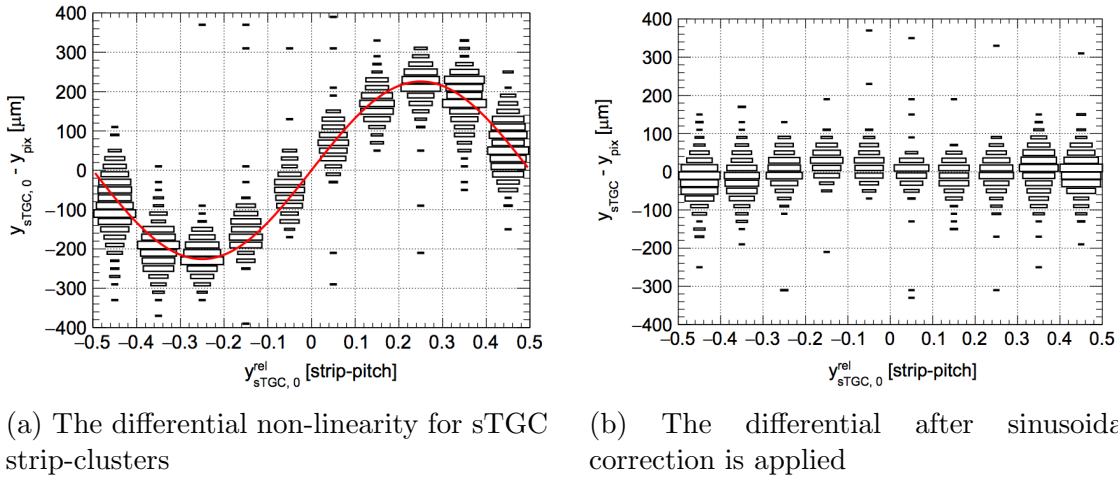


Figure 2.18: Charge distribution over strip-pitch

The charge measured on the strips of the sTGC detector results from a spatial sampling and discretization of the induced charge. The process of reconstructing the sTGC strip-cluster position from this sampling introduces a differential non-linearity effect on the reconstructed strip-cluster position. The deviation of the measured strip-cluster position from the expected position (estimated by the pixel telescope track) depends on the strip-cluster position relative to the strips. This dependence is clearly seen in the two dimensional distributions in Fig.2.18a. It shows the y -residual versus strip-cluster 439
440
441
442
443
444
445

Table 2.4: Fit parameters per cluster size

Strip-cluster multiplicity i	Amplitude parameter a_i
3	205 ± 9
4	206 ± 4
5	211 ± 5

446 position relative to the closest inter-strip gap center $y_{sTGC,0}^{rel}$. This effect is corrected
 447 using a sinusoidal function.

$$y_{sTGC} = y_{sTGC,0} - a_i \sin(2\pi y_{sTGC,0}^{rel}) \quad (2.2)$$

448 where $y_{sTGC,0}$ is the strip-cluster mean resulting from the Gaussian fit and y_{sTGC} is the
 449 corrected particle position estimator. The amplitude parameters are denoted a_i for the 3,4
 450 and 5 strip-multiplicity (cluster size). These amplitude parameters are free parameters
 451 in the fit. The values of the amplitude parameters obtained from the fit to data are
 452 compatible with being equal for the three strip-cluster multiplicity as shown in table 2.4.

453 The correction function is therefore universal and is shown in Fig.2.18a. The two
 454 dimensional distribution after the correction is applied was to be reasonably flat as shown
 455 in Fig.2.18b.

456 The alignment of the coordinate system of the pixel telescope with respect to the
 457 above-defined coordinate system of the sTGC layer also affects the measured residual
 458 distribution. A simple two-parameter model is used to account for translations and
 459 rotations of the two coordinate systems with respect to each other. Both the alignment
 460 correction and the differential non-linearity correction are included *in situ* in the analysis.
 461 The alignment correction is introduced in the model by expressing the pixel track position
 462 in the sTGC-layer coordinate system y_{pix} , is a function of the track position in the pixel
 463 telescope coordinate system x'_{pix} and y'_{pix} , and two misalignment parameters δy and ϕ_{xy} ,
 464 as follows:

$$y_{pix} = -x'_{pix} \sin \phi_{xy} + y'_{pix} \cos \phi_{xy} + \delta y \quad (2.3)$$

465 The variable δy corresponds to a misalignment along the y-axis of the sTGC coordinate
 466 system, and ϕ_{xy} corresponds to a rotation of the telescope coordinate system in the
 467 x-y plane around the z-axis of the sTGC coordinate system. Translation and rotation
 468 misalignment along and around the other axis are not taken into account in this model,
 469 since they are expected to have a small impact on the determination of the intrinsic
 470 position resolution.

471 On the figure2.19a is possible to observe the y-residual mean increase linearly as a
 472 function of the x position on the telescope called x'_{pix} , which is evidence for a small rotation
 473 between the two coordinate systems. The red line represents the correction applied to
 474 this dataset. Accounting for this correction results in a distribution that is independent
 475 of x'_{pix} on figure 2.19b.

476 After all the corrections applied, the calculations for the intrinsic resolutions are taking
 477 each layer from the sTGC and comparing the residual distribution, and fitted by a double
 478 Gaussian function, where the first one represent the core of the residual distribution and

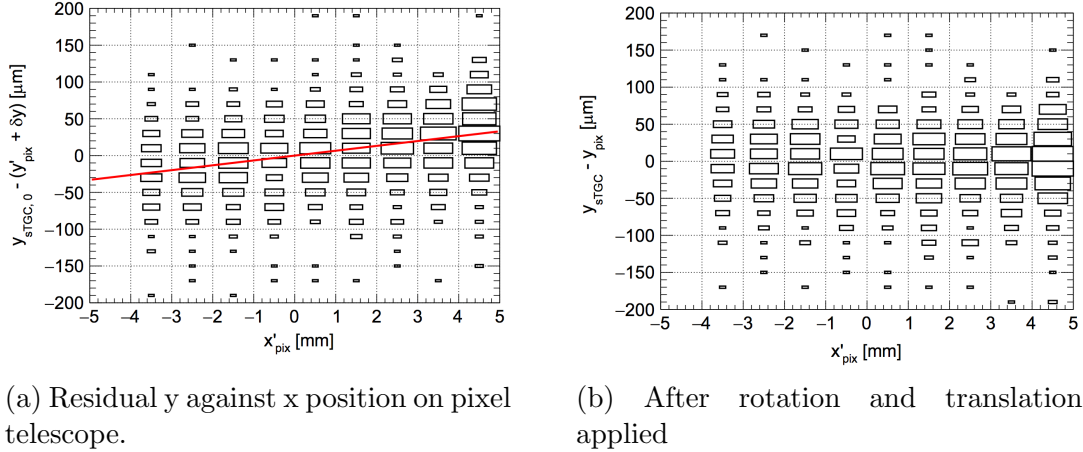


Figure 2.19: Coordinate system correction

the second is a wider Gaussian which represent some reconstructed strip-cluster from background sources.

$$\begin{aligned} F_i &= F_i(y_{sTGC,0}, y_{sTGC,0}^{rel}, x'_{pix}, y'_{pix}; \delta y, \phi_{xy}, a_i, \sigma, f, \sigma_w) \\ &= fG(y_{sTGC} - y_{pix}; 0, \sigma) + (1 - f)G(y_{sTGC} - y_{pix}; 0, \sigma_w) \end{aligned}$$

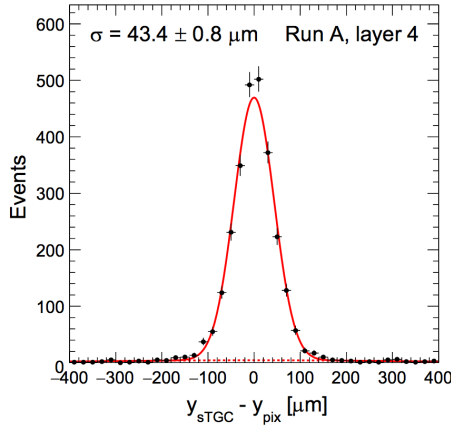
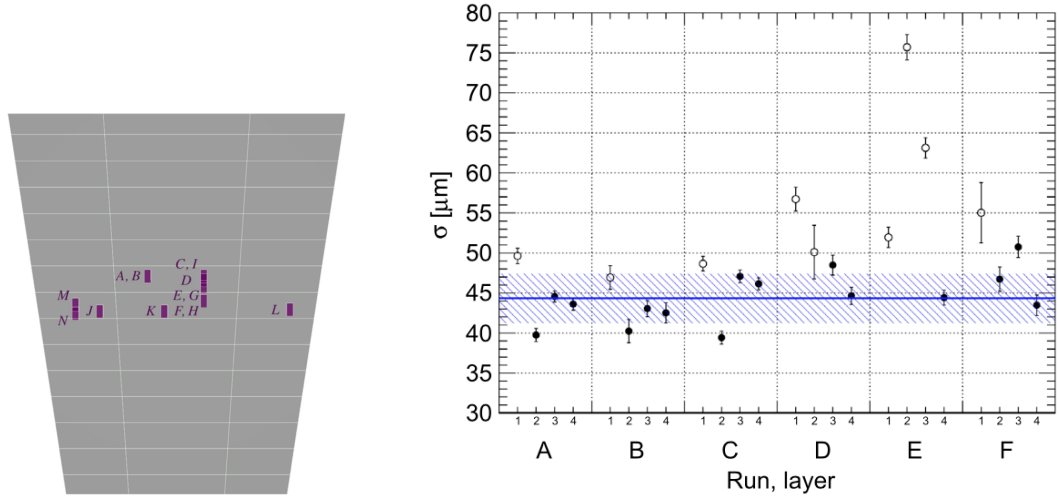


Figure 2.20: Intrinsic resolution of layer 4, respect to pixel telescope.

On figure 2.20 a set of events shows the distribution presented before with a intrinsic resolution parameter σ of about $44\mu\text{m}$ for a representative data taking run and sTGC strip-layer, where on red is the narrow Gaussian fit and on braking red line the wider Gaussian fit. The fraction of the data parameterized by the narrow Gaussian and it is typically around 95% with a RMS of about 2%. The rest of data taking runs and its beam position can be observe on figure 2.21, where the black circles represent the valid data and the open circles the runs with expected degradation due detector structure support or mis-calibrations.

479
480481
482
483
484
485
486
487
488



(a) Beam position for different data sets on sTGC

(b) Summary of intrinsic resolution for each data set and layer of sTGC

Figure 2.21: Summary of pixel telescope analysis

490 sTGC standalone analysis

491 In this analysis the correction for the differential non-linearity respect to strip-pitch
 492 obtained before is kept, however the residual distribution of the y-position is calculated
 493 from two pairwise layer of the sTGC, therefore half of the variance of this distribution
 494 correspond to our parameter to estimate the intrinsic resolution for one layer, hence
 495 $\sigma = \sigma_{\text{residual}}/\sqrt{2}$ and a strip-layer position residual distribution for a representative sTGC
 496 standalone data taking run is shown in figure 2.22a. In this graph, a intrinsic resolution
 497 of $\sigma = 40.8 \pm 0.8 \mu\text{m}$ is obtained.

498 In summary for fourteen data sets, the intrinsic resolution with this analysis is about
 499 $45 \mu\text{m}$. The white open circles on the graph 2.21 correspond to non-validate data due to
 500 wire-support position or mis-calibrations. The hash band represent the RMS spread and
 501 the blue line the average.

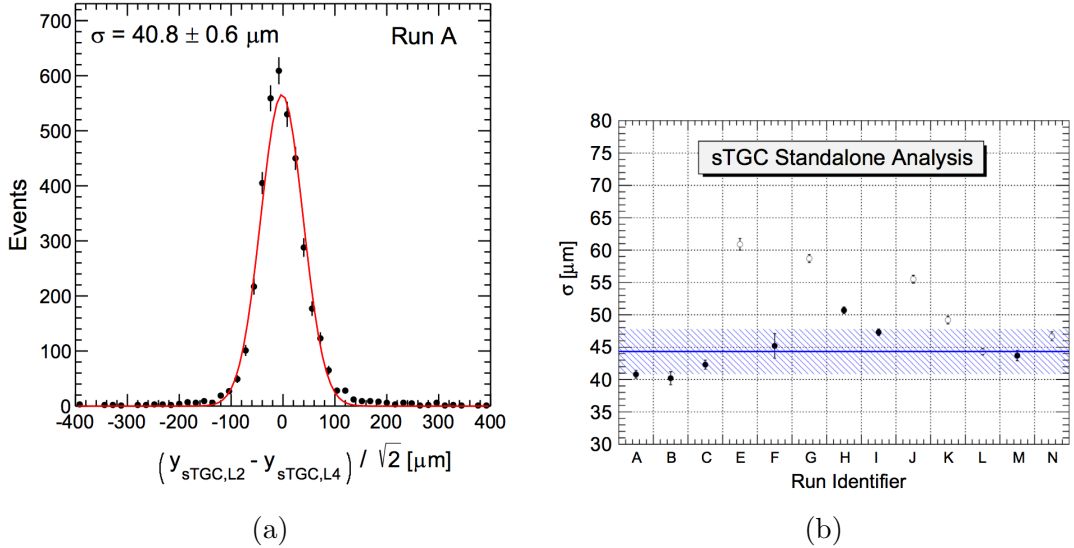


Figure 2.22

2.7. Pad efficiency

One of the new features of the small-strip Thin Gap Chamber compare to its previous version is the possibility to provide a fast trigger for the Region of Interest from the $8 \times 50 \text{ cm}^2$ pad area, where 3 out of 4 pads from a sTGC quadruplet can confirm a particle candidate, therefore a track position can be obtained from the strips within this area.

A test beam experiment was conducted at the CERN H6 beam line, using a 130 GeV muon beam of about 4 cm radius, a wider beam spot to test the characteristics of the pads. The setup is shown in figure 2.23 where the system was triggered by a set of scintillators (in blue) with a $12 \times 12 \text{ cm}^2$ coincidence area.

As explained before, for the beam tests a preliminary front-end electronics based on the VMM1 was used. This ASIC provide a Time-over-threshold signal as digital output, however is also possible to get a analog pulses. During the test beam, using the present configuration an inefficiency was observed related to small late charges from the sTGC detector which may be not well adapted to the VMM1. An efficiency of 80-90% was observe running at 100 kHz/cm^2 .

To ensure that no inefficiency was due the detector itself, the large cathode pads were used to estimate the detector efficiency, which was measured by looking at the analog output of the front-end amplifier. The efficiency of the pad n in the first layer was defined with respect to the coincidence of the trigger with a signal in the fully overlapping pad of the second layer.

Two examples from this configurations is shown on figure 2.24, on the left a two analog signals from pads are present with a ToT signal from layer 1 with about $2 \mu\text{s}$ length, meanwhile on the right picture a long ToT pulse with more than $40 \mu\text{s}$ length when the two analog signal are present. By recording hundreds of triggered events using an oscilloscope, the presence of a detector signal within the live-part of the front-end

502
503
504
505
506
507
508
509
510
511
512
513
514
515
516
517
518
519
520
521
522
523
524
525

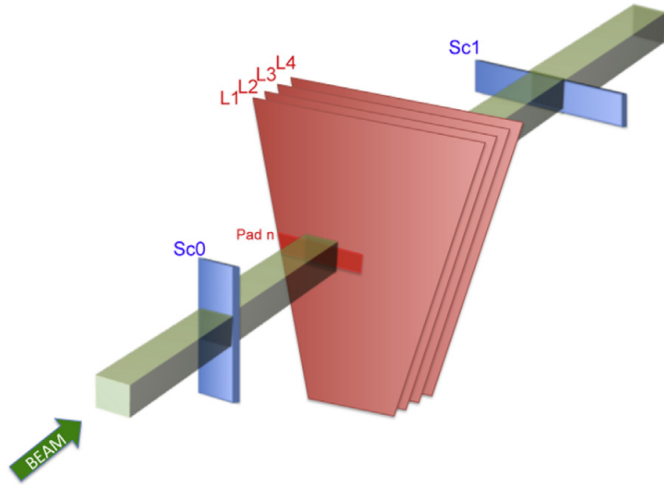
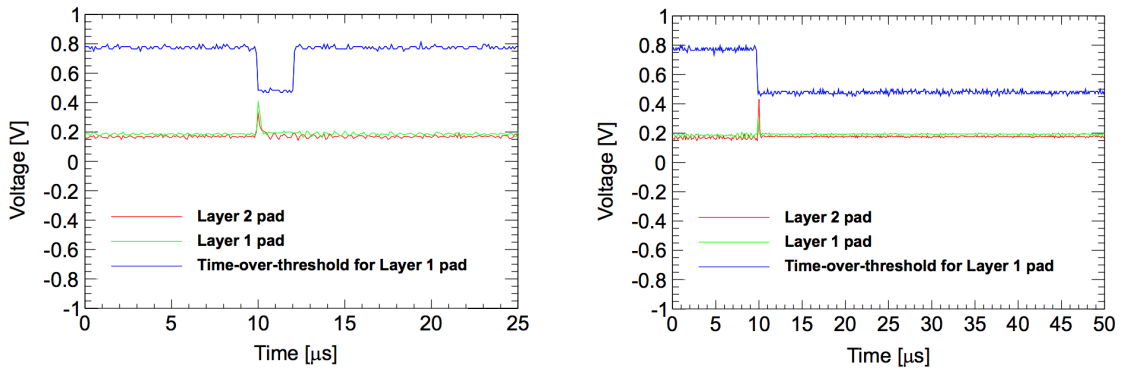


Figure 2.23: Setup for pad measurements, coincidence block on light green.



(a) ToT signal from pad L1, pad L2 as a trigger (b) Large dead time on ToT signal from pad L1

Figure 2.24: Digital and analog signal from VMM1

527 electronics (independent of the signal threshold) was checked. This test confirmed that
 528 the detector was 100% efficient.

529 **Charge sharing between pads**

530 In manner to study the transition region between pads, the scintillator coincidence
 531 triggering area and the particle beam were centered between pad n and pad $n + 1$ of the
 532 first layer, as illustrated in Figure 2.25.

533 After applying timing quality requirements on the strip and pad hits, the channel
 534 baseline values are subtracted from the analog peak values. Strip-clusters with induced
 535 charge in either 3,4 or 5 adjacent strips are selected and calibrated in the same way as
 for the Fermilab beam test. Events with a single strip-cluster in the first layer and the
 536

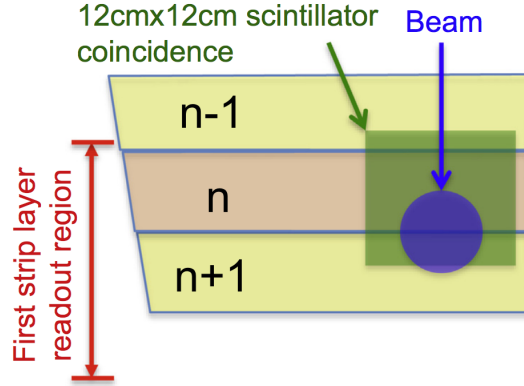


Figure 2.25: Pad region transition scheme

second layer are selected. The strip-cluster position (mean of the fitted Gaussian) in the first layer is used to define the position of the particle going through the detector. The events are further required to contain a hit above threshold on either pad n or pad $n + 1$. The charge fraction (F) is defined using the analog peak values (P) of the two adjacent pads:

$$F = \frac{P_n - P_{n+1}}{P_n + P_{n+1}} \quad (2.4)$$

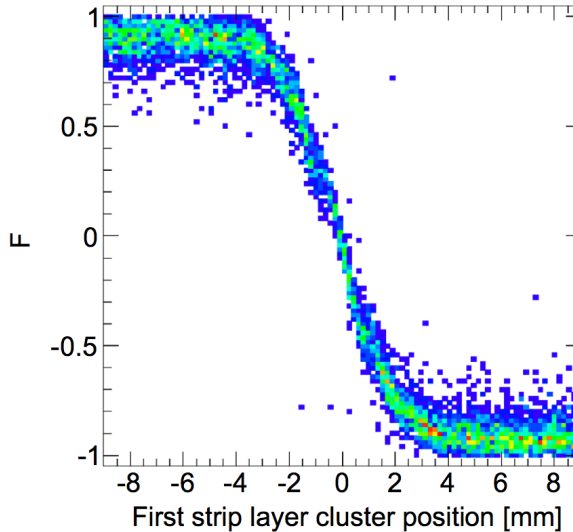


Figure 2.26: Charge Sharing distribution

Figure 2.26 shows the charge fraction as a function of the position with respect to the center of the transition region, where the two pads share more than 70% of the induced charge, spans about 4mm.

545 2.8. Summary

546 The spatial resolutions and pad efficiency results has been published in “Performance
547 of a full-size small-strip thin gap chamber prototype for the ATLAS new small wheel
548 muon upgrade”

- 549 ■ A improvement of the dead time on the electronic readout must be done
- 550 ■ A cosmic muon test is remaining to provide the efficiency map for the module 0
- 551 ■ A test with muons with high background must be made with module 0, with the
new readout electronics.

552

3. High count rate γ -ray spectroscopy with Brilliance380

553

554

3.1. Introduction

555

- Problem faced in chapter 2, with high radiation facility. 556
- Explain the attempt to get reference about this issue 557
- Device to be used BriLLance 380 558
- characterization 559

3.2. Counter Limit

560

Limit of pulse recognition, refer paper high rate... 561

3.3. High Radiation Source

562

Description of Cesium source, flow estimation for GIF++, 563

3.4. Data Analisys

564

3.4.1. Multiple hits

565

how to handle it? 566
567

3.4.2. Wavelets

568

Introuction to Wavelets 569
Discrete Wavelet Transform 570

571

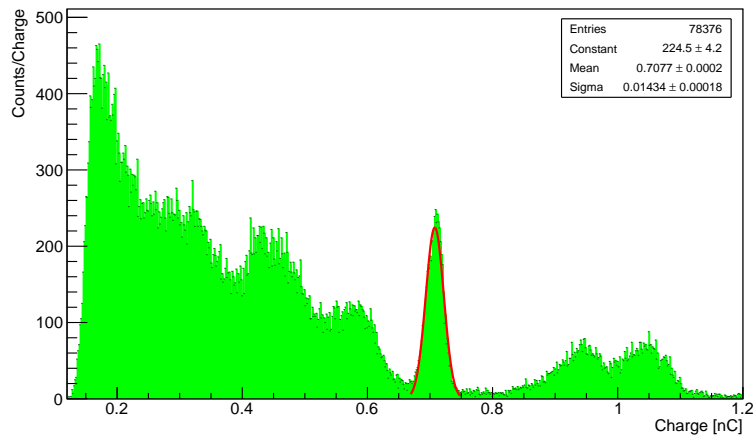


Figure 3.1: Selfcount spectrum

572 **3.4.3. Peak identification**

573 Chosing Wavelet function for peak identification

574 Heavy ion paper, peak identification

575

576 **3.5. Results**

577 Show multiple pulse in window, and peak identification, cases...

578 **3.5.1. Spectrum**

579 Spectrum for different rates (attenuation filters)

580 Spectrum with multiple pulse, using peak identification and pattern recognition.

581

582 **3.5.2. Gamma Flux Rates**

Rate estimation, compare with gain and rate measured with Scaler.

583

4. Synchrotron radiation detector for e^- tagging

584

585

4.1. Introduction

586

Many high energy experiments require pure electron beams. Despite the steady improvement of the beam lines, contamination below a level of few % is very difficult to achieve. An example is the NA64 experiment at CERN in which it is mandatory to suppress hadron and muon contamination in the electron beam since such particles can generate irreducible background processes mimicking the experimental signature of a dark photon [ref](#). NA64 uses 100 GeV electrons from beam lines provided by the Super Proton Synchrotron (SPS) at CERN which is one of the best existing beam lines at this energy in terms of beam purity [ref](#).

587

588

589

590

591

592

593

594

4.2. NA64 experiment

595

The NA64 experiment is a fixed-target experiment at the CERN SPS combining the active beam dump and missing energy techniques to search for rare events.

596

597

A fully hermetic detector placed on the H4 beam line has been built with the primary goal to search for light dark bosons (Z') from dark sector that are coupled to photons, e.g. dark photons (A'), or sub-GeV Z' coupled only to quarks. In some cases the Z' is coupled only to μ or τ , so we call the Z' the dark leptonic gauge boson. The experiment is also capable to search for $K_L \rightarrow invisible$ decay, which is complementary to $K^+ \rightarrow \pi^+ + \nu\nu$, and invisible decays of π_0, η, η', K_S mesons.

598

599

600

601

602

603

The advantage of this approach is that the sensitivity (or number of signal events) of the experiment is roughly proportional to the Z' coupling squared ε^2 , associated with the Z' production in the primary interaction in the target, while in a classical beam dump experiment, it is proportional to ε^4 , one ε^2 came from the Z' production, and another ε^2 is either from the probability of Z' decays or their interactions in a detector located at a large distance from the beam dump.

604

605

606

607

608

609

The sensitivities of these two methods depend on the region under study in the (ε^2, m_Z) parameter space, background level for a articular process, available beam intensity, etc. [\[Beam intensity\]](#)

610

611

612

613 In some cases, much less running time and primary beam intensity are required to
 614 observe a signal event with our approach.

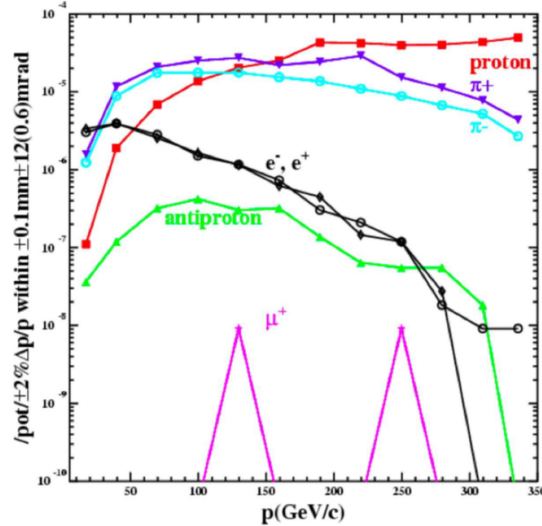


Figure 4.1: Particle production rate at H4 beam line from target T2

615 One of the main background sources in the experiment is related to the possible
 616 presence of the low-energy tail in the energy distribution of beam electrons. This tail was
 617 observed during irradiation of the setup by the 100 GeV electron beam without switching
 618 on the deflecting magnet**electron tail**. This tail is caused by the electron interactions
 619 with a passive material, e.g. as entrance windows of the beam lines, residual gas, etc...
 620 Another source of low energy electrons is due to the pion or muon decays in flight in
 621 the beam line. The uncertainties arising from the lack of knowledge of the dead material
 622 composition in the beam line are potentially the largest source of systematic uncertainty
 623 in accurate calculations of the fraction and energy distribution of these events. Hence,
 624 the sensitivity of the experiment could be determined by the presence of such electrons
 625 in the beam, unless one takes special measures to suppress this background. To reject
 626 these background sources at high energies by using standard techniques, e.g. threshold
 627 Cerenkov counters, is practically impossible.

628 To improve the high energy electrons selections and suppress background from the
 629 possible admixture of low energy electrons, we use a tagging system utilizing the synchrotron
 630 radiation (SR) from high energy electrons in a dipole magnet, installed upstream of the
 631 detector. The basic idea is that, since the critical SR photon energy is $(\hbar\omega)_\gamma^c \propto E_0^3$, the
 632 low energy electrons in the beam could be rejected by using the cut, e.g. $E_\gamma > 0.3(\hbar\omega)_\gamma^c$,
 633 on the energy deposited in the SR detector.

4.2.1. Physics Motivation

634

$$\mathcal{L} = \mathcal{L}_{SM} - \frac{1}{4} F'_{\mu\nu} F'^{\mu\nu} + \frac{\epsilon}{2} F'_{\mu\nu} F^{\mu\nu} + \frac{m_{A'}^2}{2} A'_\mu A'^\mu + i\bar{\chi}\gamma^\mu \partial_\mu \chi - m_\chi \bar{\chi}\chi - e_D \bar{\chi}\gamma^\mu A'_\mu \chi \quad (4.1)$$

Standard Model.

635

 $g_\mu - 2$ muon anomaly

636

637

4.2.2. Dark Photon signal

638

U(1) broken symmetry \rightarrow massive dark photon

639

type of mixing coupling constant and sub-GeV mass connect with g2 muon anomaly. How to detect him?

640

641

Visible decay

642

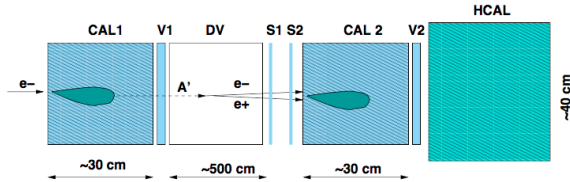
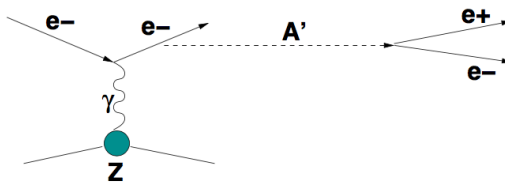


Figure 4.2

$$S_{A'} = \text{CAL1} \cdot \overline{V1} \cdot S1 \cdot S2 \cdot \text{CAL2} \cdot \overline{V2} \cdot \text{HCAL} \quad (4.2)$$

Figure 4.3: Diagram illustrating the massive A' production in the reaction $e^-Z \rightarrow e^-ZA'$ of electrons scattering off a nuclei (A, Z) with the subsequent A' into an e^+e^- pair.

Invisible decay

643

The method of the search is the following. The incident electron energy absorption in the ECAL is accompanied by the emission of bremsstrahlung A' s in the reaction $eZ \rightarrow$

644

645

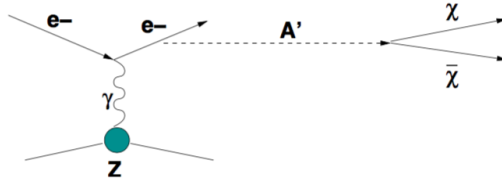


Figure 4.4: Production rate at H4 beam line

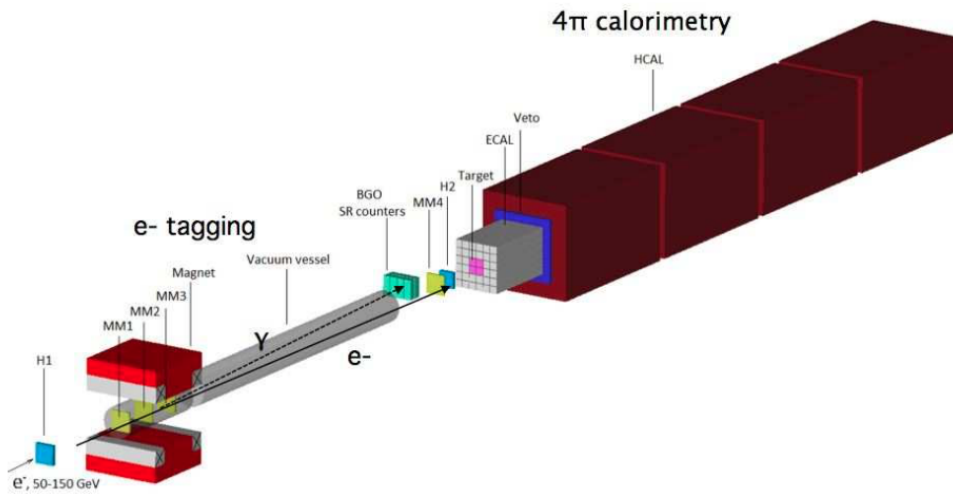


Figure 4.5

646 eZA' of electrons scattering on nuclei, due to the $\gamma - A'$ mixing. The diagram for the A'
 647 production in the reaction is shown in 4.4.

648 The reaction typically occurs in the first few radiation length (X_0) of the calorimeter.
 649 The part of the primary beam energy is deposited in the ECAL, while the remaining
 650 fraction of the total energy is transmitted by light dark matter decay particles χ through
 651 the rest of the detector. The χ penetrates the ECAL, veto V and the HCAL without
 652 interactions resulting in the missing-energy signature in the detector.

653 The occurrence of $A' \rightarrow \text{invisible}$ decays produced in e^-Z interactions would appear
 654 as an excess of events with a single electromagnetic shower in the ECAL1, Fig. 4.7, and
 655 zero energy deposition in the rest of the detector (V and HCAL), above those expected
 656 from the background sources. The signal candidate events have the signature:

$$S_{A'} = H1 \cdot H2 \cdot \text{ECAL}(E_{\text{ECAL}} < E_0) \cdot \bar{V} \cdot \text{HCAL} \quad (4.3)$$

657 and should satisfy the following selection criteria:

- 658
 - 659 ■ The momentum of the incoming particle track should correspond to the beam momentum.
 - 660 ■ The starting point of (e-m) showers in the ECAL should be localized within a few

first X_0 s.

661

- The lateral and longitudinal shapes of the shower in the ECAL are consistent with an electromagnetic one. The fraction of the total energy deposition in the ECAL is $f < 0.5$.
662
663
664
- No energy deposition in the V and HCAL.
665

To improve the primary high energy electrons selection and additionally suppress background from the possible presence of low energy electrons in the beam typically with energy $E_e < 0.5E_0$ (see below), one use a high energy e^- tagging system utilizing the synchrotron radiation (SR) from high energy electrons in a dipole magnet, as schematically shown in Fig. 4.7.
666
667
668
669
670

4.2.3. Detector

671

The A' production is a rare event. For the interesting parameter range it is expected to occur with a rate 10^{-9} with respect to the ordinary photon production rate. Hence, its observation represents a challenge for the detector design and performance.
672
673
674

The experimental setup specifically designed to search for the A' production in the reaction (4) of high-energy electron scattering off nuclei in a high density target T is schematically shown in Fig. 3. The experiment employs the upgraded H4 electron beam line at the CERN SPS described in details in Ref.[21]. The beam is designed to transport the electrons with the maximal intensity $\simeq (3 - 4) \cdot 10^6$ per SPS spill in the momentum range between 50 GeV/c to 150 GeV/c that could be produced by the primary proton beam of 450 GeV/c with the intensity up to a few 10^{12} protons on target. The electrons are produced by protons impinging on a primary beryllium target and transported to the detector inside the evacuated beam-line tuned to an adjustable beam momentum.
675
676
677
678
679
680
681
682
683

The hadron contamination in the electron beam is $\pi/e < 10^{-2}$ and the size of the beam at the detector position is of the order of a few cm².
684
685

The detector shown in Fig. 3 utilizes upstream magnetic spectrometers (MS) consisting of dipole magnets and a low-material-budget tracker, which is a set of Micromegas chambers , MM1-MM4, allowing the reconstruction and precise measurements of momenta for incident electrons [22]. It also uses the scintillating counters S0, S1 and hodoscopes H1 and H2 to define the primary beam, and the active target T, which is the central part of the high-efficiency hodoscopic electromagnetic calorimeter (ECAL) used for the accurate measurement of the recoil electron energy from the reaction (4). Downstream the target the detector is equipped with high-efficiency forward veto counter V, and a massive, completely hermetic hadronic calorimeter (HCAL). Three straw-tubes chambers, MUON1-MUON3, located between the HCAL modules are used for the final-state muon(s) identification. The modules serve as a dump to completely absorb and detect the energy of hadronic secondaries produced in the electron interactions $e^-A \rightarrow \text{anything}$ in the target. In order to suppress backgrounds caused by the detection inefficiency the HCAL must be longitudinally completely hermetic [18, 19]. To enhance its hermeticity, the HCAL thickness is chosen to be $\simeq 30\lambda_{\text{int}}$ (nuclear interaction lengths). The 15 m long
686
687
688
689
690
691
692
693
694
695
696
697
698
699

700

701 vacuum vessel between the magnet and the ECAL is installed to avoid absorption of the
 702 synchrotron radiation photons detected at the downstream end of the vessel by the array
 703 of BGO crystals for the effective tagging of the incoming beam electrons [18].

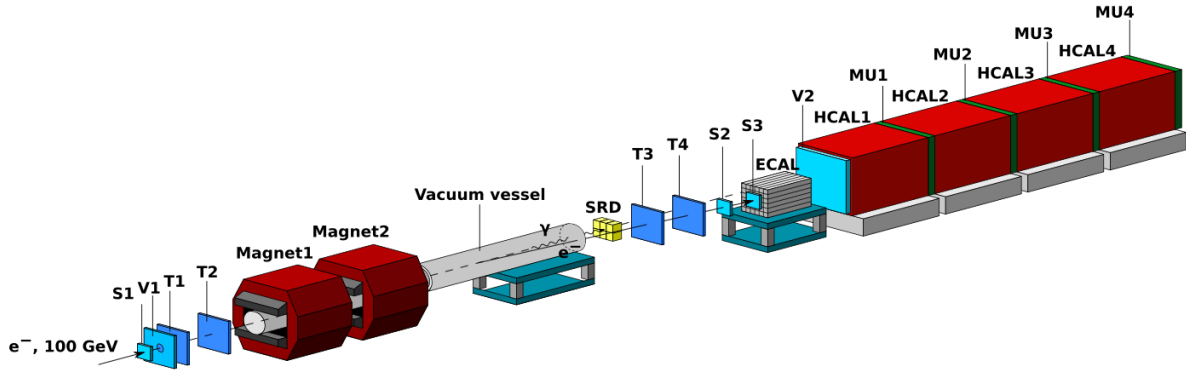


Figure 4.6: Schematic illustration of the setup to search for $A' \rightarrow \text{invisible}$ decays with 100GeV e^- at H4 beam line. the incident electron energy absorption in the ECAL is accompanied by the emission of *bremsstrahlung* A 's in the reaction $eZ \rightarrow eZA'$ of electron scattering on nuclei, see Diagram interaction. The part of the primary beam energy is deposited in the ECAL, while the remaining fraction of the total energy is transmitted by the decay dark matter particles through the rest of the detector resulting in the missing energy signature in the detector.

704 4.3. Synchrotron Radiation Detector

705 A charged particle in a magnetic field moves in a circular motion emitting photons
 706 along its trajectory due to the basic principles of electrodynamics. Both quantum and
 707 classical theory of synchrotron radiation (SR) are well understood 4.10. In the range of
 708 interest for our experiment both treatments are equivalent and we can therefore use the
 709 classical approximation for our calculations. The total power S emitted per unit length
 710 by a relativistic charged particle of energy E with mass M and with bending radius R in
 711 a magnetic field B perpendicular to its velocity is given by:

$$712 S = \frac{q^2 c}{6\pi} \frac{1}{(Mc^2)^4} \frac{E^4}{R^2} \quad (4.4)$$

712 where q is the charge of the particle and c the speed of light. Since the emission angle
 713 of the synchrotron is proportional to the inverse of the Lorentz factor γ , the photons are
 714 emitted tangentially to the particle trajectory.

715 Hence under a circular acceleration, an charged particle, e.g. an electron, emits
 716 synchrotron radiation and the energy radiated per particle per turn being

$$\Delta E = \frac{e^2 \beta^3}{3\epsilon_0 R} \left(\frac{E}{mc^2} \right)^4 \quad (4.5)$$

Putting the numerical values for ε_0 and e , and setting $\beta = 1$

717

$$\Delta E = 0.08856 \frac{E^4}{R} \quad (4.6)$$

where ΔE is in MeV, E is in GeV and R is in meters. Thus for relativistic π^- 's and e^- 's of the same energy, the energy loss is $(m_e/m_{\pi^-})^4 \sim 10^{-10}$ times less for a π . This would be the case if the particles propagate in an ideal vacuum. However, in a real experimental setup, vacuum windows, residual gas, beam counters such as scintillators and trackers result in interactions of the incoming particles with material. Therefore, the suppression factor when crossing materials is limited by the emission of secondary electrons with enough kinetic energy (several MeV) to leave a synchrotron-like signal in the detector. Although most of the energy transfer due to ionization for heavy charged particles is only a few keV, rare high energy transfer is possible. The distribution of such secondary electrons with kinetic energy $T \gg I$, where I is the mean excitation energy of the atom/molecule, for a particle with velocity β and charge z passing through a material with atomic number Z , mass number A and thickness dx is described by ref:

$$\frac{d^2N}{dTdx} = \frac{1}{2} K z^2 \frac{Z}{A} \frac{1}{\beta^2} \frac{F(T)}{T^2} \quad (4.7)$$

The constant K is defined as $K = 4\pi N_A r_e^2 m_e c^2$ where N_A is the Avogadro's number, r_e is the classical electron radius and m_e the electron mass. $F(T)$ is a spin-dependent factor, which in our case for $T \ll W_{max}$ is very close to unity. W_{max} is the maximal energy transfer in a single collision to the electron:

For a π^- at GeV, W_{max} is roughly 1GeV which covers completely the energy range where synchrotron radiation is emitted.

4.3.1. BGO

The idea to use scintillator crystals as synchrotron radiation detector for tagging electrons has been tested before[14]. As a first option the experiment use the $\text{Bi}_4\text{Ge}_3\text{O}_{12}$ (BGO) crystals because of its properties. The detector consists of 8 hexagonal crystals with an external diameter of 55 mm and a length of 200 mm. The crystals are grouped into two modules. Each crystal is wrapped in Teflon tape for efficient light collection and it is glued to an ETL 9954 photomultipliers(PMT).

The BGO has a density of 7.13 g/ cm^3 and because of the high atomic number of the bismuth component ($Z = 83$) it has one of the largest probability per unit volume for photoelectric absorption of gamma rays. ref13SRDpaper. The light yield of about 8500 photons/MeV coupled to the transportation losses and quantum efficiency of the PMT gives an energy resolution of about 17% (FWHM) at 1.27 MeV (measured with a ^{22}Na radioactive source.

748

736

737

738

739

740

741

742

743

744

745

746

747

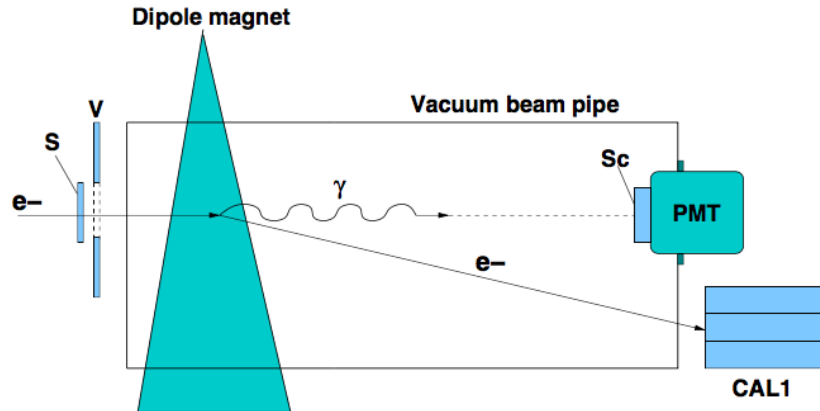


Figure 4.7: The scheme of the additional tagging of high energy electrons in the beam by using the electron synchrotron radiation in the bending magnetic dipole. The synchrotron radiation photons are detected by a γ -detector by using scintillator as BGO crystals, LYSO crystals or different configuration with Pb+Sc. All these options are viewed by a high quantum efficiency PMT or SiPM. The beam defining counters are also shown.

749 4.3.2. Pb+Sc

750 4.3.3. LYSO

751 Readout

752 The readout consist of 50 Multi-pixel Photon Counter (MPPC) [ref](#), distributed into
 753 25 per axis. Within each axis, 5 MPPC are grouped with similar gain to share the same
 754 bias voltage. On one axis the signal is read it from each single MPPC, while on the other
 755 one, only two weighted signals are taken. The amplification circuit is shown in [fig](#) [amp.](#)
 756 [circuit](#).

757 It is an array of 25x25 of 4x4x45mm³ LYSO crystals and read-out with Wave Length
 758 Shifter (WLS) fibers. Each crystal is a Cerium doped lutetium (Lu_{1.8}Y_{0.2}SiO₅ : Ce), a
 759 based scintillation crystal that offers high density and a short decay time. Having similar
 760 density than BGO can offer improvement in energy resolution, light output and better
 timing due to its short time decay constant (see table 4.1). 761

Property	LYSO	BGO
Density [g/m ³]	7.1	7.1
Attenuation length for 511 keV [cm]	1.2	1.0
Decay time [ns]	41	300
Energy Resolution %	8.0	12.0
Light output, photons per keV	32	9

Table 4.1: Property comparison LYSO and BGO crystals

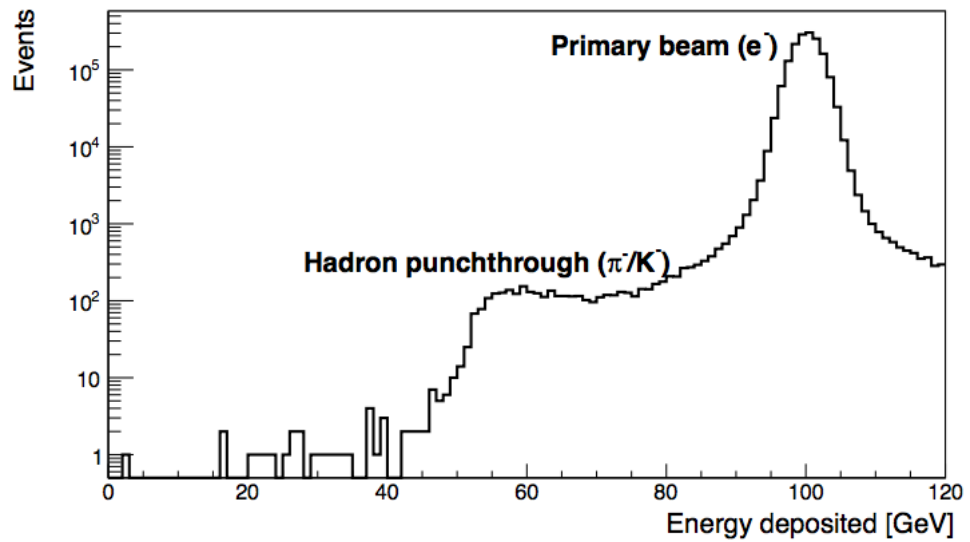


Figure 4.8

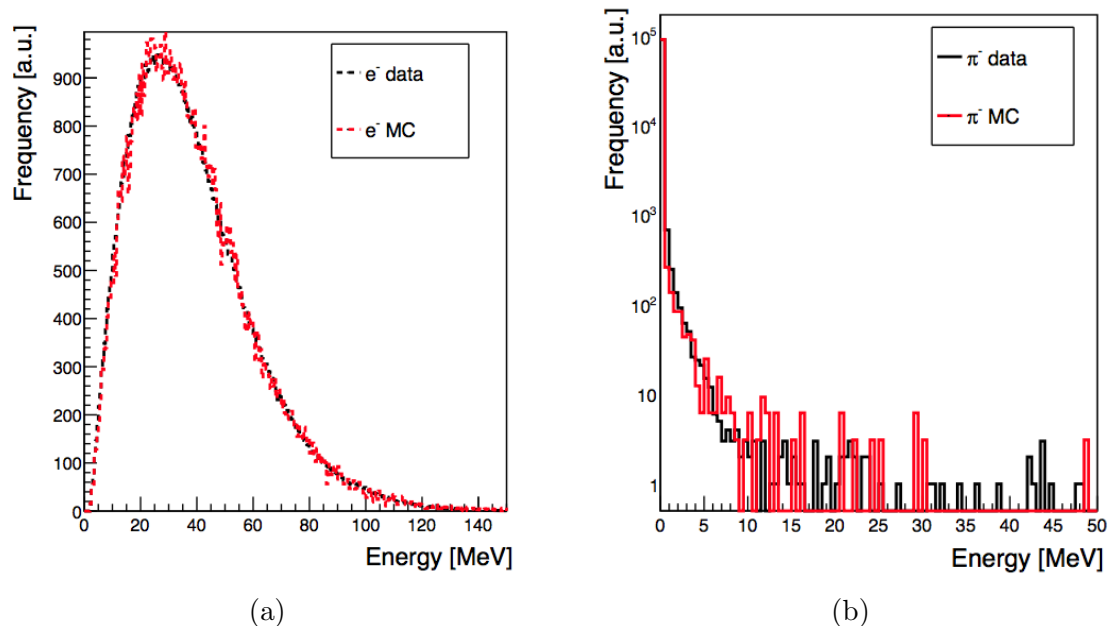


Figure 4.9

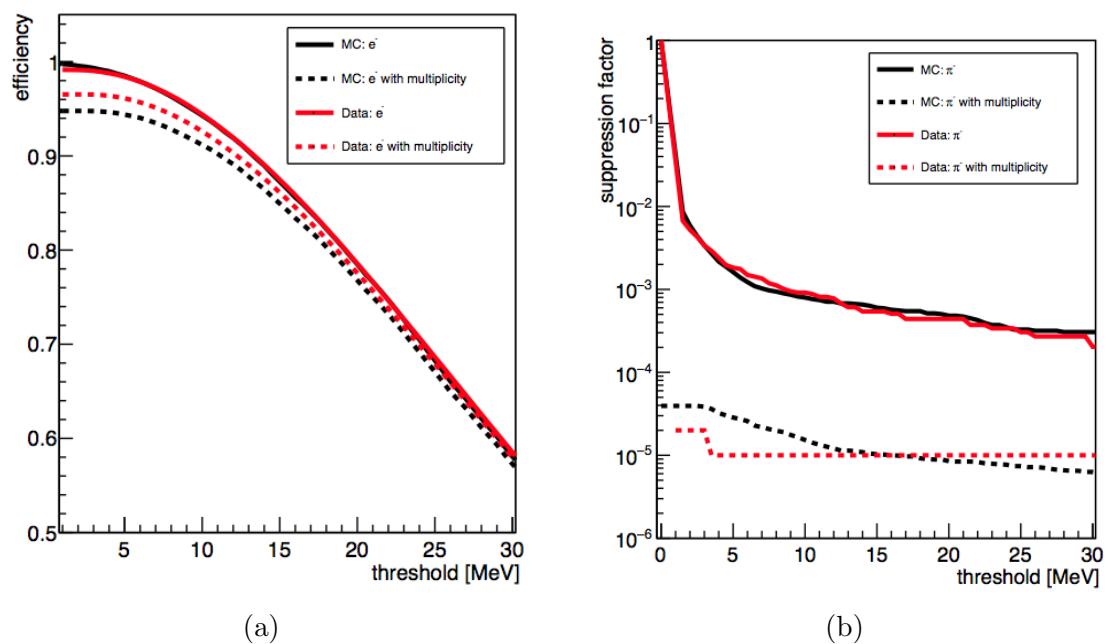


Figure 4.10

4.4. Calibration

762

X-axis equalization

763

MIP calibration on X axis

764

Explain how the amplitude is obtained, how the pedestal are calculated. Plot example

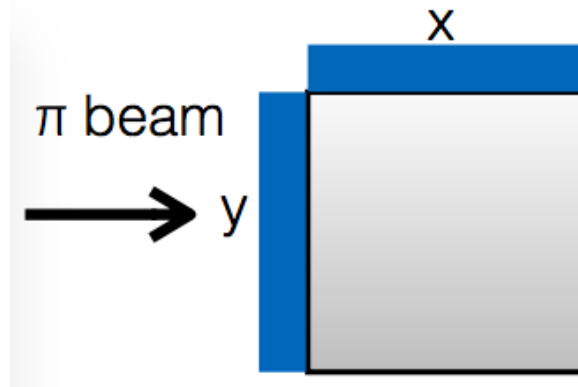


Figure 4.11

single channel, with Vavilov pdf fit. Plot pedestal, mean and sigma per channel. Plot channel mip, sigma and percentage sigma/mu per channel.

765

766

767

Y-axis equalization

768

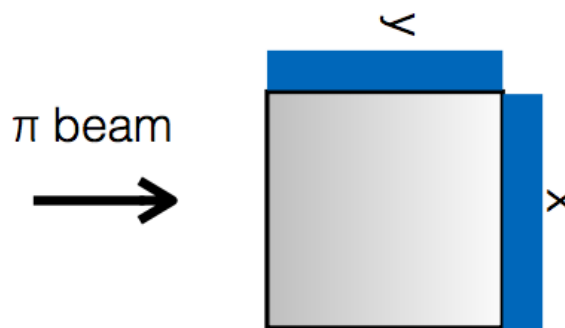


Figure 4.12

Since the Y-axis has two weighted signals as readout, the readout boards must be exchanged. Afterwards the detector is turn over 90 degrees. Now the beam hits all the crystals along the x-axis as the scheme shows 4.12.

769

770

771

Again the mean energy deposited on each strips it must be the energy loss by one MIP across 4mm, the width of one crystal. Plot channel mip, sigma and percentage sigma/mu per channel.

772

773

774

775 **Z-axis configuration**

776 Finally the beam hits the detector as its standard configuration. The weighted signals
777 can be correlated between each other

778 MIP on Z axis

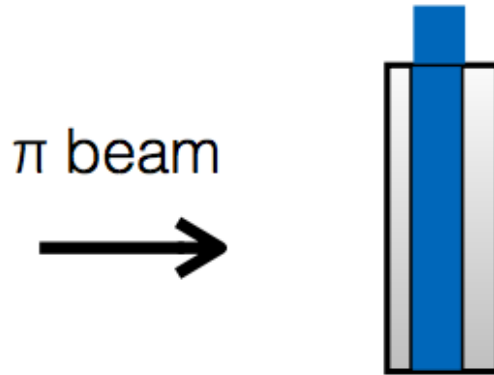


Figure 4.13

779

780 **4.5. Energy and time resolution**

781 Time is defined respect to the first counter S1, and calculated with constant fraction
782 method where:....

783 The temporal resolution on a single channel is shown in ..

784

785 **4.6. Hadron rejection**

786 **4.7. Experimental Results**

4.8. Summary

787

5. Conclusion

788

A. Appendix

789

A.1. Mechanical Measurements sTGC Module 0

790

A.2. PMT RT7525 Data Sheet

791

A.3. NA64 Experiment:Data structure

792

A.4. NA64 Experiemnt:DAQ system

793

Bibliography

794

- [1] ATLAS collaboration, “*Observation of a new particle in the search for the Standard Model Higgs boson with the ATLAS detector at the LHC*”, Physics Letters B **716** (2012) 1–29. 795
796
797
- [2] CMS collaboration, “*Observation of a new boson at a mass of 125 GeV with the CMS experiment at the LHC*”, Physics Letters B **716** (2012) 30–61. 798
799
- [3] G.Mikenberg et al., *Thin-gas gap chambers for hadronic calorimetry*, Nucl. Instr. and Meth. A **265** (1988) 223–227. 800
801
- [4] V.Smakhtin et al., *Thin Gap Chamber upgrade for SLHC: Position resolution in a test beam*, Nucl. Instr. and Meth. A **598** (2009) 196–200. 802
803
- [5] S.Majeski, *A Thin wire chamber operating in a high multiplication mode*, Nucl. Instr. and Meth A **217** (1983) 265–271. 804
805
- [6] W. Blum, *Particle Detection with Drift Chambers*. Springer, 2008. 806
- [7] Garfield++, *Project web page*, <http://garfieldpp.web.cern.ch/garfieldpp/>. 807
- [8] R. Veenhof, *GARFIELD, recent developments*, Nucl. Instr. and Meth A **419** (1998) 808
726–730. 809
- [9] F.Sauli, *Principle of operation of multiwires proportional and drift chambers*. CERN, 1977. 810
811
- [10] *sTGC construction’s manual*, <https://edms.cern.ch/document/1399978/1>. 812
- [11] *Mini-X Gun Datasheet*, <http://www.amptek.com/pdf/minix.pdf>. 813
- [12] GIF++, *The new Gamma Irradiation Facility*, <https://espace.cern.ch/sba-workspace/gifpp/>. 814
815
- [13] M. Y. O.Sasaki, *ASD IC for the thin gap chambers in the LHC Atlas Experiment*, IEEE Transactions on Nuclear Science **46** (1999) 1861–1864. 816
817
- [14] R. Cryttenden, *Synchrotron radiation detector for tagging electrons*, Nucl. Instr. and Meth A **276** (1989) 643–646. 818
819